1949

Localization in quantum chromodynamics on the lattice

Thesis for the Degree of Doctor of Philosophy (PhD)

Réka Á. Vig

Supervisor:
Dr. Tamás G. Kovács

UNIVERSITY OF DEBRECEN
Doctoral Council of Natural Sciences and Information Technology
Doctoral School of Physics

Debrecen, 2021

Hereby I declare that I prepared this thesis within the Doctoral Council of Natural Sciences and Information Technology, Doctoral School of Physics, University of Debrecen in order to obtain a PhD Degree in Natural Sciences at Debrecen University.
The results published in the thesis are not reported in any other PhD theses.

Debrecen, 2021. june 14.

Vig Réka Ágnes
candidate

Hereby I confirm that Réka Ágnes Vig candidate conducted her studies with my supervision within the Particle Physics Doctoral Program of the Doctoral School of Physics between 2017. and 2021. The independent studies and research work of the candidate significantly contributed to the results published in the thesis.
I also declare that the results published in the thesis are not reported in any other theses.
I support the acceptance of the thesis.

Debrecen, 2021. june 14.

Dr. Kovács Tamás György
supervisor

Localization in quantum chromodynamics on the lattice

Dissertation submitted in partial fulfilment of the requirements for the doctoral (PhD) degree in physics

Written by Réka Ágnes Vig certified physicist

Prepared in the framework of the Doctoral School of Physics of the University of Debrecen
(Particle physics programme)

Dissertation advisor: Dr. Tamás György Kovács

The official opponents of the dissertation:

Dr. ....
Dr. ....

The evaluation committee:

chairperson:	Dr.	.....
members:	Dr.	.....
	Dr.	.....
	Dr.	.....
	Dr.	.....

The date of the dissertation defence: .....

Acknowledgements

First I would like to thank my supervisor, Dr. Tamás G. Kovács, who led me through over my master and PhD studies. Without his help this work would not have been accomplished. His excellent insights and the useful discussions through the years helped me to become a young researcher.

I would like to thank my beloved life partner, Ákos, for his support and patience and that he took care of our baby daughter while I was working on my thesis. I thank my other family members for providing me a great home environment during my work.

I am grateful to my friends for inspiring discussions about physics and other interesting topics about the world.

I thank the Budapest-Wuppertal collaboration for letting us use their code and Pittler Ferenc for providing us help with the code.

Contents

Chapter 1

Introduction

Quantum chromodynamics (QCD) is the fundamental quantum field theory of the strong interaction, the force that holds together the basic constituents of hadrons. It is a gauge theory, which means that its Lagrangian has a symmetry with respect to local gauge transformations of the fields. In QCD, there is a symmetry with respect to the local transformations with the non-abelian gauge group SU(3). The interaction acts between color charged particles, namely quarks and gluons. In color space quarks are represented by fields of three dimensional complex vectors and they transform as a color triplet under the fundamental representation of the group SU(3). There is no privileged basis of the quarks, which means one can transform the basis locally without changing the physics. Gluons are represented by the gauge fields of the theory that describe how the basis changes between different space-time points. Gluons are gauge bosons that mediate the strong force, similarly to photons in quantum electrodynamics (QED). They transform as octets under the adjoint representation of the group SU(3), i.e. there are eight gluons with different color charges. As gluons also carry color charge, they interact with themselves, in contrast to abelian gauge theories, like QED, where photons do not have an electric charge.

QCD is a well established theory by growing experimental evidence, however there are still unanswered questions about the nature of the strong interaction. At low energies, quarks are in a color neutral bound state, i.e. singlets under SU(3) transformations. In this state quarks cannot be observed individually, only in confined forms in hadrons. This is called color confinement. At higher temperatures, QCD matter undergoes a rapid crossover [1] in which quarks and gluons become liberated, forming a quark-gluon plasma (QGP) state. In contrast with

the hadronic phase, quarks are deconfined in the QGP, hence we call this transition deconfinement. This is an interesting phenomenon in QCD, the details of which, to this day, are not fully understood.

It is also known that at the low temperature regime eigenmodes of the quark Dirac operator are delocalized in space [2]. This changes when the temperature is raised. Eigenmodes at the lowest part of the Dirac spectrum become spatially localized [3–6]. The appearance of the first localized modes happens at a well defined temperature, somewhere in the crossover temperature region of deconfinement [6].

It was also shown, that localization is accompanied also by the restoration of the approximate chiral symmetry [4, 5], that is spontaneously broken at low temperature. Thus there are three phenomena that happen at the same temperature region; deconfinement, localization and the chiral restoration. Therefore one can ask the question of what is the relationship among these three phenomena. It is conceivable that one of them might governs the other two. It was already suggested, that chiral restoration might be driven by a localization transition [3]. However, detailed understanding of the QCD transition is still pending. Investigations about the relationship of localization with deconfinement are also needed to understand the whole picture. Hence one of the main interests in our studies is to discover the possible connection between deconfinement and localization.

Another interesting question is what mechanism causes that the quark modes with the lowest eigenvalues become spatially localized. Gauge fields, that are nontrivial solutions of the Euclidean Yang-Mills equations of motions can be related to the appearance of localized eigenmodes at the origin of the Dirac spectrum. On these topologically nontrivial gauge field configurations, there are regions of space-time where the gauge field is locally very strong. These localized lumps of gauge field are called instantons (or antiinstantons). On a gauge background with one the instanton, the Euclidean Dirac operator has an exact zero eigenmode [7]. It was shown that the corresponding eigenmode is localized on the instanton [8].

At low temperature, according to the instanton liquid model (for a review see [9]), the gauge field is densely populated by instantons and antiinstantons. Gauge configurations of the instanton liquid are not exact solutions of the Euclidean equations of motions, therefore the Dirac operator has only approximately zero eigenvalues. The mixing of the close eigenvalues causes a finite spectral density around the ori-

gin. This is connected to spontaneous breaking of the chiral symmetry, through the Banks-Casher relation [10]. At high temperature, above the QCD crossover, instantons are believed to form a dilute gas. In this case approximate zero modes of instantons are too far from each other to sufficiently mix. Therefore the low end of the spectrum becomes depleted, resulting in chiral symmetry restoration.

Since instantons have the above mentioned role in the chiral transition and their presence is accompanied by localized quark modes with approximate zero eigenvalues, it is crucial to examine their connection to the phenomenon of localization. Therefore the other goal of our studies was to find out whether localization can be explained by instanton related localized eigenmodes of small magnitude.

The strong coupling is large at the temperature region of the crossover, therefore it can only be examined with non-perturbative methods. Lattice field theory is a non-perturbative approach to QCD, that provides a mathematically well-defined framework to study the transition region of the strongly interacting matter. Therefore our studies were performed by using lattice gauge theory.

The structure of the thesis is the following. In chapter 2 I introduce the basics of how one can study QCD on the lattice. In chapter 3 I discuss the new results of our investigation. In section 3.2 I show how we calculated the critical point of localization with staggered fermions in the quenched approximation [11,12]. I summarize this result in the first thesis point. Section 3.3 includes our results [13] of the critical point of localization calculated by using another fermion discretization, the overlap Dirac operator, which is the topic of the second thesis point. In section 3.4 I discuss our studies of the topological objects of the gauge field. In section 3.4.2 I show how we determined the ratio of the number of topology related small eigenmodes and the total number of all localized modes [11, 14], which is summarized in the third thesis point. We showed that the topological objects can be described as a dilute non-interacting gas above the critical temperature [15, 16]. These results are discussed in section 3.4.3 and in the fourth thesis point. In chapter 4 I draw the conclusions and indicate future directions. Then I close the thesis with a summary in English and a summary in Hungarian.

Chapter 2

Lattice regularized QCD

This chapter dedicated to the introduction of the theoretical background that served as the basis of our research, which I will present in the following chapter. Specifically I will show the path integral formalism, which is the quantization tool of lattice field theory and why its mathematical structure makes it possible to simulate the theory with computers. Then I will deal with the lattice discretization of the action of the gauge field and two different discretizations of the fermion field that we used in our work. And lastly I will present the finite temperature transition of the QCD matter, which was the subject of our investigation during the research. In writing this chapter, I relied mainly on the References [17–19].

QCD is the quantum field theory of the strong interaction, that describes the quarks and the force mediators, the gluons with continuous fields. When we work with a quantized field theory we have to introduce a regularization method to avoid divergences during the calculations of observables. There are different regulator parameters that can be used to exclude the scales from the calculations that our theory cannot describe. For example a small parameter added to the dimension of space-time is often used in perturbation theory. After removing the regulator parameter we can get finite results. The only regularization method that works for large gauge couplings and therefore can be used outside of perturbation theory is lattice regularization. In this case we consider that the fields only exist at discrete points of the space-time, for example at the grid-points of a four dimensional cubic lattice. The edge length of the cubes, a is called the lattice constant. In this case a is the regulator parameter that we have to remove at the end of the calculations. This means taking the continuum limit i.e. a goes to zero.

Usually we approach the continuum limit through a path on which we require some experimentally known physical parameters to remain fixed. In QCD these parameters could be hadron masses and decay constants. On the lattice the parameters of the Lagrangian density are in lattice units, i.e. they are dimensionless and they are called bare parameters. These should be renormalized to match the measurements of reality. This practically means that we tune the bare parameters, while keeping the quantities in physical units constant as we approach the continuum limit. This procedure defines the line of constant physics in the space of bare parameters.

We can quantize a field theory by canonical quantization or with the path integral method. The former means to require the field operator and its time-derivative to obey special commutation relations. In the case of the path integral quantization (discussed in the next section) we integrate over all classical field configurations weighted with an exponential factor, which has the classical action at its exponent. To define these integrals first we have to discretize the fields in space and time so it is natural to use the lattice regularization with this quantization. There is another property of the path integral formulation which makes its use advantageous in lattice QCD. This is its mathematical equivalence with statistical mechanics, which I will show on the example of the scalar field in the next section. This structure makes it possible to simulate quantum field theory on a finite size hypercubic lattice with the Monte Carlo method. The results of this thesis are based on data generated by such algorithm.

2.1 Path integral on the lattice

2.1.1 Path integral of the scalar field

Now I will show the lattice regularized path integral on the simplest example, the real scalar field, ϕ. In quantum field theory if we want to get information about what happens with the field we calculate correlation functions or the so called Green functions. The probability of a field excitation (a particle) propagating from one space-time point to another is calculated by the two point Green function. It is defined by the functional expectation value of the product of two field functions

at different space-time points x_1 and x_2

$$G(x_1, x_2) = \frac{1}{Z} \int \mathcal{D}\phi \ \phi(x_1)\phi(x_2) e^{iS[\phi]}. \tag{2.1}$$

This equation is written in $\hbar = 1$ unit system, which will be used from now. $S[\phi]$ is the classical action which is determined by the Lagrangian density of the system and Z is a normalization factor. The integral $\int \mathcal{D}\phi$ means integrating over the set of all possible field configurations in every space-time point, which will be defined later in this section. The fluctuating factor e^{iS} in the integrals makes the evaluation of the Green functions questionable. We solve this by rotating the time variable by 90° in the complex plane, called the Wick-rotation. Technically this means a multiplication by the imaginary unit, $t \to it \equiv \tau$. The action contains an integration over time and the Lagrangian density depends on the second order time derivative of the fields

$$S[\phi(x,t)] = \int dt d^3x \ \mathcal{L}(\partial_t^2 \phi(x,t), \partial_x^2 \phi(x,t), \phi(x,t)). \tag{2.2}$$

For better transparency I wrote out the time variable and denoted the space variables with a concise form x. Performing a variable exchange from t to τ we get the Euclidean action S_E, which is related to the action as

$$S[\phi(x,t)] = iS_E[\phi(x,t)]. \tag{2.3}$$

This step leads to the elimination of i from the exponent, i.e. the fluctuating factor becomes a real exponential

$$e^{iS[\phi(x,t)]} \to e^{-S_E[\phi(x,t)]}. \tag{2.4}$$

We call the action Euclidean, because by changing to imaginary time the metric becomes Euclidean instead of Minkowski. This is because τ in contrast with t behaves in the same way as the space variables.

Now we come back to define the integral over all of the possible field configurations. In the case of continuous fields the integral is infinite dimensional, since there is an infinite number of degrees of freedom. We can make it finite dimensional by using lattice regularization, which will be the case through the whole thesis from now on. If we put the function on a finite lattice Λ, we only allow the field to exist at discrete points of Λ and it means a finite number of degrees of freedom. Now the measure can be written as

$$\mathcal{D}\phi = \prod_{n \in \Lambda} d\phi(n), \tag{2.5}$$

where we denoted the lattice sites by n. With this nomenclature we can write the two point Green function on the lattice in the following way

$$G(n,m) = \frac{1}{Z}\int \mathcal{D}\phi\ \phi(n)\phi(m)e^{-S_E[\phi(n)]};\ n,m \in \Lambda. \tag{2.6}$$

To get the probability interpretation we have to choose the normalization factor as

$$Z = \int \mathcal{D}\phi\ e^{-S_E[\phi(n)]}, \tag{2.7}$$

which is also called the partition function. The expectation value of any other $O(\phi(n))$ observable on the lattice is calculated in the following way

$$\langle O(\phi(n))\rangle = \frac{1}{Z}\int \mathcal{D}\phi\ O(\phi(n))e^{-S_E[\phi(n)]}. \tag{2.8}$$

The similarity with the statistical mechanical expression of the expectation value is conspicuous

$$\langle O\rangle_{stat} = \frac{1}{Z_{stat}}\sum\ Oe^{-\beta H_{stat}}. \tag{2.9}$$

H_{stat} and Z_{stat} denote the Hamiltonian and the partition function of the statistical mechanical system and $\beta = 1/k_BT$ is the inverse temperature, where k_B is the Boltzmann constant. Other consequences of this analogy will be discussed in section 2.4.

Finally I show the discretized form of the action of the scalar field on the Euclidean lattice. We can discretize the derivatives by taking the central differences[1]

$$\partial_\mu\phi \to \frac{\phi(n+\hat{\mu}) - \phi(n-\hat{\mu})}{2a}, \tag{2.10}$$

where $\hat{\mu}$ means a vector with magnitude a pointing in the μ direction. With this form of the derivatives we obtain the Euclidean action of the scalar field in the form

$$S_E[\phi] = a^4\sum_{n\in\Lambda}\frac{1}{2}\sum_{\mu=1}^{4}\left(\frac{\phi(n+\hat{\mu}) - \phi(n-\hat{\mu})}{2a}\right)^2 + \frac{1}{2}m^2\phi^2(n) + V(\phi(n)), \tag{2.11}$$

[1]Other discretizations could be also used for the derivatives as they reproduce the continuum theory in the continuum limit, however the rate of convergence to the continuum limit can depend on the particular discretization.

where $V(\phi(n))$ is the potential and m denotes the mass parameter of the scalar field. On the lattice the four dimensional space-time integral became a sum over all lattice points, multiplied by the fourth power of the lattice constant.

So far we have seen how to get the lattice discretized form of the action in the case of the real scalar field, which we used in the path integral formula. In the next section I will write down the discretized action of QCD and the corresponding lattice path integral. In

2.1.2 QCD path integral

For the construction of the QCD lattice action, as it is a gauge theory, we need the to discretize the gauge field A_μ as well as the fermion fields ψ, $\bar{\psi}$. I will sketch the lattice discretized forms similarly as I did with the scalar field in the previous section. The more detailed discussion of the construction of the gauge and fermion fields on the lattice will be written down further in sections 2.2 and 2.3.

The continuum Euclidean QCD action is a four dimensional integral of the QCD Lagrangian density $\mathcal{L}_{QCD}$

$$S[\psi(x), \bar{\psi}(x), A_\mu(x)] = \int d^4x \ \mathcal{L}_{QCD}. \tag{2.12}$$

From now on I will write everything in Euclidean metric and for simplicity I omit the subscript E. Putting the fields on the lattice the integral becomes a sum. Using the central differences for the derivatives and constructing a gauge invariant quantity from the gauge field we obtain an expression of the lattice discretized action. For transparency I separate the action into fermionic S_F and gluonic S_G parts

$$S = S_G + S_F \tag{2.13}$$

$$S_G[U_\mu(n)] = \frac{2}{g^2} \sum_{n\in\Lambda} \sum_{\nu<\mu} Re \ tr[\mathbb{1} - U_{\mu\nu}], \tag{2.14}$$

$$\begin{aligned} S_F[\psi(n), \bar{\psi}(n), U_\mu(n)] &= a^4 \sum_f \sum_{n\in\Lambda} \bar{\psi}^f(n) \times \\ \times \left(\sum_\mu \gamma_\mu \frac{U_\mu(n)\psi^f(n+\hat{\mu}) - U_{-\mu}(n)\psi^f(n-\hat{\mu})}{2a} + m^f \psi^f(n) \right). \end{aligned} \tag{2.15}$$

This form of the gluonic action is called the Wilson gauge action. The factor g is the coupling strength of the gauge and fermion fields. The matrix-valued variables U_μ are elements of the SU(3) gauge group and they replace A_μ on the lattice. $U_\mu(n)$, also called the link variable, means a gauge rotation that connects the sites n and $n+\hat{\mu}$ in the lattice. Hence $U_\mu(n)$ can be considered to live on the links between the neighboring sites, pointing in the μ direction. The $U_{-\mu}(n)$ notation means the link variable connects the sites n and $n-\hat{\mu}$ therefore points in the $-\mu$ direction. The relation between $U_{-\mu}(n)$ and the gauge rotation that points in the positive μ direction from the site $n-\hat{\mu}$ on the same link is $U_{-\mu}(n) = U_\mu^\dagger(n-\hat{\mu})$. The Hermitian conjugation also means taking the inverse of the gauge rotation as the link variables are unitary matrices $U_\mu^\dagger(n) = U_\mu^{-1}(n)$. Finally the meaning of $U_{\mu\nu}$, called the plaquette variable, is a product of the link variables on the smallest closed loop on the lattice, which we call the plaquette

$$U_{\mu\nu} = U_\mu(n)U_\nu(n+\hat{\mu})U_{-\mu}(n+\hat{\mu}+\hat{\nu})U_{-\nu}(n+\hat{\nu}). \tag{2.16}$$

A more detailed description of the link variables and their connection to the continuum gauge field will be given in the next section. In the fermionic action f is the flavor index and m^f denotes the mass parameter of a fermion with a given flavor. The three summations run over all of the fermion flavors, the lattice sites and the four Dirac indices. Note that we constructed the covariant derivative by using the product of link variables and fermion fields, therefore the fermionic action has a dependence on $U_\mu(n)$ too. We will see that there will be problems with this naively discretized form of the fermionic action. The problems and different solutions will be introduced in section 2.3.

The partition function of QCD using the fermionic and the gluonic actions reads

$$Z = \int \mathcal{D}[\psi,\bar{\psi}]\mathcal{D}[U_\mu]\; e^{-S_F[\psi(n),\bar{\psi}(n),U_\mu(n)]}e^{-S_G[U_\mu(n)]}, \tag{2.17}$$

where the path integral measure is defined by the product measures

$$\mathcal{D}[\psi,\bar{\psi}] = \prod_{n\in\Lambda}\prod_{f,\alpha,a} d\psi^f_{a,\alpha}(n)d\bar{\psi}^f_{a,\alpha}(n),\;\; \mathcal{D}[U] = \prod_{n\in\Lambda}\prod_{\mu} dU_\mu(n), \tag{2.18}$$

where α and a are spinor and color indices. The integration measure over the SU(3) group manifold of the link variables is the so called Haar measure. I note here that the products of the fermion measures

are also nontrivial, because ψ and $\bar{\psi}$ are so called Grassmann variables, which means they obey the anti-commuting relations of fermions. The expectation value of an observable in QCD with the path integral is given by

$$\langle O(\psi(n), \bar{\psi}(n), U_\mu(n)) \rangle = \\ = \frac{1}{Z} \int \mathcal{D}[\psi, \bar{\psi}] \mathcal{D}[U_\mu] \; O(\psi(n), \bar{\psi}(n), U_\mu(n)) e^{-S_F} e^{-S_G}. \tag{2.19}$$

This is the simplest form of QCD on the lattice, however other discretizations could be used also, as long as they reproduce the right continuum form in the continuum limit. For the fermionic action there will be a need to use improved discretizations to solve the problem of the so called fermion doubling, discussed in section 2.3. In the next section I will show that the lattice QCD action introduced in this section is gauge invariant and reproduces the appropriate continuum form in the naive continuum limit.

2.2 SU(3) gauge theory on the lattice

In this section the lattice discretized form of the SU(3) gauge field and the gluonic and interaction parts of the QCD action will be discussed in details.

First I show the relation between the continuum gauge field and the SU(3) link variables of the lattice. In the continuum a quantity that connects two points x and y in space-time along a curve is the so called gauge transporter

$$T(x, y) = P \; e^{i \int_x^y ds_\mu A_\mu(s)}, \tag{2.20}$$

where P means path ordering and the summation convention for μ was used. Since we work in Euclidean time, the upper and lower Dirac indices are equivalent and therefore I will only use lower indices in the expressions. As the link variables are defined as rotations that connect the fermion field in two different points on the lattice, we identify them with the gauge transporter connecting the sites n and $n + \hat{\mu}$

$$U_\mu(n) = T(n, n + \hat{\mu}). \tag{2.21}$$

Since A_μ, used in the continuum theory, is an element of the lie algebra of SU(3), $U_\mu(n)$ is an SU(3) group element which is the fundamental variable of the gluon field on the lattice.

Putting the gauge field this way on the lattice ensures the gauge invariance of the lattice action, which we require when building a gauge theory on the lattice. Let us consider a local gauge transformation $V(n)$ of the fermion fields

$$\begin{aligned} \bar{\psi}^f(n) &\to \bar{\psi}^f(n)V^\dagger(n), \\ \psi^f(n) &\to V(n)\psi^f(n). \end{aligned} \tag{2.22}$$

If one inserts it into the fermionic part of the QCD action (2.15), it can be seen that the mass term is obviously invariant under local gauge transformations, as $V^\dagger(n)V(n) = 1$. As U_μ is an element of the gauge group it will transform under local gauge transformations like

$$U_\mu \to V(n)U_\mu(n)V(n+\hat{\mu})^\dagger. \tag{2.23}$$

Using this transformation property of the link variables, all of the gauge transformation matrices will be canceled in the interaction part of the fermionic action also. Therefore the form (2.15) of the lattice discretized fermionic action is invariant under local gauge transformations.

We can also show that in the continuum limit the original form of the continuum fermionic action is restored. To this end we use an approximation of the link variable

$$U_\mu(n) = e^{iaA_\mu(n)} + \mathcal{O}(a). \tag{2.24}$$

Since the continuum limit means that the lattice constant tends toward zero, we can expand (2.24) into its Taylor series

$$U_\mu(n) = \mathbb{1} + iaA_\mu(n) + \mathcal{O}(a^2), \quad U_{-\mu}(n) = \mathbb{1} - iaA_\mu(n-\hat{\mu}) + \mathcal{O}(a^2). \tag{2.25}$$

By using the following forms

$$\psi^f(n \pm \hat{\mu}) = \psi^f(n) + \mathcal{O}(a), \; A_\mu(n-\hat{\mu}) = A_\mu(n) + \mathcal{O}(a), \tag{2.26}$$

in the interaction part of the fermionic action, then S_F becomes

$$S_F = ia^4 \sum_f \sum_{n\in\Lambda} \bar{\psi}^f(n) \sum_\mu \gamma_\mu \frac{\psi^f(n+\hat{\mu}) - \psi^f(n-\hat{\mu})}{2a} + \tag{2.27}$$

$$+\gamma_\mu A_\mu(n)\psi^f(n) + m^f\psi + \mathcal{O}(a).$$

Then taking the limit $a \to 0$ the sum over all lattice sites becomes a four dimensional integral, the central difference becomes a differential and the continuum counterpart of the fermionic action is reconstructed

$$S_F^{cont} = \int d^4x \; \bar{\psi}(x)(\gamma_\mu(\partial_\mu + iA_\mu(x)) + m)\psi(x). \tag{2.28}$$

I now show the same for the gluonic part of the QCD action, i.e that it is gauge invariant and that the correct form of the continuum action could be restored. Taking the trace of any closed loop $\mathcal{L}$ built from the product of link variables

$$L[U] = tr\left[\prod_{(n,\mu)\in\mathcal{L}} U_\mu(n)\right] \tag{2.29}$$

is a gauge invariant object. Using the transformation property (2.23) of the link variables in the product, the gauge transformation matrices cancel each other, except on the site n_0 where the loop is started. Then after gauge transformation (2.29) become

$$L[U'] = tr\left[V(n_0)\prod_{(n,\mu)\in\mathcal{L}} U_\mu(n)V^\dagger(n_0)\right] = tr\left[\prod_{(n,\mu)\in\mathcal{L}} U_\mu(n)\right] = L[U], \tag{2.30}$$

where we used that the trace is invariant under cyclic permutations. The Wilson gauge action (2.14) is built up by summing the traces of all plaquettes, the simplest closed loops on the lattice, therefore it is also gauge invariant. The concrete form of the Wilson action guarantees that the continuum form of the action is recovered when taking the limit $a \to 0$. Since the gauge field is non-abelian, we show this by using the Baker-Campbell-Hausdorff formula

$$e^A e^B = e^{A+B+\frac{1}{2}[A,B]+\ldots} \tag{2.31}$$

where A and B are Lie algebra elements and the dots indicate higher commutators of them. Inserting the Taylor expansion of the gauge field up to second order, $A_\nu(n+\hat{\mu}) = A_\nu(n) + a\partial_\mu A_\nu(n) + \mathcal{O}(a^2)$, into the expression of the plaquette variable (2.16) and using (2.31) it reads

$$U_{\mu\nu}(n) = \exp(ia^2(\partial_\mu A_\nu(n) - \partial_\nu A_\mu(n) + i[A_\mu(n), A_\nu(n)]) + \mathcal{O}(a^3)) \tag{2.32}$$

$$= \exp(ia^2 F_{\mu\nu}(n) + \mathcal{O}(a^3)),$$

where $F_{\mu\nu}(n)$ is the field strength tensor. Inserting this into the Wilson gauge action (2.14) one finds

$$S_G[U] = \frac{a^4}{2g^2} \sum_{n\in\Lambda} \sum_{\mu,\nu} tr[F_{\mu\nu}(n)^2] + \mathcal{O}(a^2), \tag{2.33}$$

where we used the Taylor expansion of (2.32). By taking the limit $a \to 0$, we get the continuum expression of the gauge action

$$S_G[A] = \frac{1}{2g^2} \int d^4x \; tr[F_{\mu\nu}(x)^2]. \tag{2.34}$$

In the next section I will discuss the case of pure gauge theory. Using a lattice gauge theory without fermions makes the simulations much easier, with the advantages that essential properties of full QCD like color confinement, the finite temperature transition (discussed in section 2.4) and the appearance of nontrivial topological objects are also present. However, there is a difference compared to full QCD, namely that in the pure gauge theory, the deconfinement is a genuine phase transition and not a crossover. Our main goal was to study the connection between the deconfining transition and localization (introduced later in chapter 3), for which we used the quenched approximation, discussed in the following section.

2.2.1 Quenched approximation

The quenched approximation means that we only work with the self-interacting gauge field without taking the contribution of the fermions into account, i.e. it is the case of pure gluodynamics. For the mathematical construction of this approximation first let us rewrite the fermionic part of the QCD action into a compact form

$$S_F[\psi, \bar{\psi}, U] = a^4 \sum_f \sum_{n,m\in\Lambda} \bar{\psi}^f(n) D^f(n|m) \psi^f(m). \tag{2.35}$$

$D^f(n|m)$ means the lattice Dirac operator of the quarks of a given flavor. The partition function is a Gaussian integral over the anti-commuting quark fields. This can be performed as

$$Z_F = \int \mathcal{D}[\psi, \bar{\psi}] \; e^{-S_F} = \prod_f \det(D^f[U]). \tag{2.36}$$

The determinant is depending only on the U variables, since the fermion fields are integrated out. Then the QCD partition fuction can be written in the form

$$Z = \int \mathcal{D}[\psi, \bar{\psi}, U] \; e^{-S_G} e^{-S_F} = \int \mathcal{D}[U] \; e^{-S_G} \prod_f \det(D^f[U]). \quad (2.37)$$

The quenched approximation means setting $\det(D^f[U]) = 1$ for all flavors. This gives a great simplification in simulations with the Monte Carlo method, because one can update the gauge field only by the gluonic action and do not have to compute the fermion determinant.

The physical meaning of neglecting the fermion determinants is taking the limit of infinitely heavy virtual quarks, which therefore cannot be generated as quark-antiquark pairs from the fermionic vacuum, i.e. forbidding the generation of closed quark loops. This can be seen if we write the Dirac operator in the form $D_0^f(U) + m^f$, with the notation $D_0^f(U)$ meaning the massless Dirac operator. The determinant can be neglected if we take the limit of infinite masses. In this case $D_0^f(U)$ becomes infinitely small compared to the masses, therefore the determinant will not depend on the gauge field anymore. This means the determinant will be a constant for the path integral, which appears in the numerator and also in the denominator in the calculations of the observables, therefore disappears from the expressions. More detailed discussion by presenting the hopping parameter expansion can be read in the literature [17, 19].

2.3 Fermions on the lattice

In this section I will introduce the problem of fermion doubling on the lattice, which can be seen as the appearance of unwanted poles in the fermion propagator. By adding an extra term to the fermionic action the doublers can be eliminated and we will arrive to a new improved action, called the Wilson fermion action. Another solution to the doubling problem is the so called staggered fermion action, which reduces the number of the poles to four instead of sixteen when we work in a four dimensional space-time. Although these quark formulations provide a solution to the doubling problem they also involve the violation of the chiral symmetry. While the Wilson fermion action explicitly breaks the chiral symmetry, by adding an extra term to eliminate the spurious poles, in the staggered formulation a remnant chiral symmetry

remains. With the so called overlap discretization (discussed in section 2.3.3), the action has exact chiral symmetry on the lattice, however in this case one has to deal with the problem of much slower numerical evaluation than in the two former cases.

To obtain the fermion propagator we have to compute the inverse of the lattice Dirac operator of the fermion fields. The calculations are easier in momentum space, thus first we take the Fourier transform of $D(m|n)$. For simplicity first we discuss the case of free quarks, which means the gauge field is set to its trivial value $U_\mu(n) = \mathbb{1}$. In this case the naive Dirac operator is given by

$$D(n|m)_{\alpha,\beta} = \sum_\mu \gamma_{\mu,\alpha,\beta} \frac{\mathbb{1}\delta_{n+\hat{\mu},m} - \mathbb{1}\delta_{n-\hat{\mu},m}}{2a} + m\delta_{\alpha,\beta}\delta_{n,m}, \tag{2.38}$$

where α, β are Dirac indices. To simplify the expressions the sum over the flavors is omitted, as the doubling problem is present in the same form for all flavors, only the mass term is different. The Fourier transform of this operator reads

$$\tilde{D}(p|q) = \frac{1}{N_\Lambda} \sum_{n\in\Lambda} e^{-i(p-q)na} \sum_\mu \gamma_\mu \frac{e^{iq_\mu a} - e^{-iq_\mu a}}{2a} + m\mathbb{1}, \tag{2.39}$$

where N_Λ is the number of all lattice sites. The sum of the first exponential over the lattice points is the exponential representation of the Dirac delta function $\delta(p-q)$ on the lattice, which eliminates the q dependence of the Fourier transformed Dirac operator, which therefore takes the form

$$\tilde{D}(p) = \frac{i}{a} \sum_\mu \gamma_\mu \sin(ap_\mu) + m\mathbb{1}. \tag{2.40}$$

The momentum components p_μ are restricted to the first Brillouin zone $(-\frac{\pi}{a}, \frac{\pi}{a}]$ on a finite lattice. Since $\tilde{D}(p)$ is diagonal in momentum space the inverse can be taken easily and we get

$$\tilde{D}^{-1}(p) = \frac{-\frac{i}{a}\sum_\mu \gamma_\mu \sin(ap_\mu) + m\mathbb{1}}{\frac{1}{a^2}\sum_\mu \sin^2(ap_\mu) + m^2}. \tag{2.41}$$

In the massless case the propagator (2.41) has a pole at $p = 0$ and also if the momentum takes values at the corners of the Brillouin zone. This means it produces a pole if the momentum components are either zero or $\frac{\pi}{a}$. These are two poles for each μ direction, hence the name

doublers. For d dimensions, the propagator has 2^d poles, which for the four dimensional space-time means 16 massless particles. When taking the naive limit $a \to 0$ and setting the masses to zero in (2.41), we get the correct continuum form of the massless quark propagator

$$\tilde{D}^{-1}(p)^{cont} = \frac{-i \sum_\mu \gamma_\mu p_\mu}{p^2}. \tag{2.42}$$

The continuum propagator has only one pole at $p = 0$. This means that on the lattice the propagator produces 15 unphysical quarks. This causes problems if we do lattice calculations for finite lattice spacings or even in the continuum limit as the propagator governs the behavior of the n-point functions. For example with the naive discretization the real space lattice quark propagator (the two point function for free fermions) is given by the inverse Fourier transform of (2.41). In the massless case it reads

$$\left\langle \bar{\psi}(n)|\psi(m)\right\rangle = D^{-1}(n|m) = \frac{1}{N_{\tilde{\Lambda}}} \sum_{p\in\tilde{\Lambda}} e^{ia(n-m)p} \frac{-\frac{i}{a}\sum_\mu \gamma_\mu \sin(ap_\mu)}{\frac{1}{a^2}\sum_\mu \sin^2(ap_\mu)}, \tag{2.43}$$

where the sum runs over the points in the first Brillouin zone of the momentum space lattice. Thus as a goes toward zero, the quark propagator still gets finite contributions from the sines when p takes values near the corners of the Brillouin zone.

This phenomenon comes from the naive lattice discretization of the derivative in the Dirac operator of the quarks. Thus a solution, given by Wilson, is to add a derivative term, $-\frac{a}{2}\partial_\mu\partial_\mu \sim \Box$, in lattice discretized form to the naively discretized fermionic action. On the lattice it reads as

$$S_W = S_F + a^4 \sum_{n\in\Lambda} \bar{\psi}(n) a \sum_\mu \frac{2\psi(n) - U_\mu(n)\psi(n+\hat{\mu}) - U_{-\mu}(n)\psi(n-\hat{\mu})}{2a^2}, \tag{2.44}$$

where we wrote out the Wilson term. Then the lattice Dirac operator in momentum space becomes

$$\tilde{D}(p) = \frac{i}{a}\sum_\mu \gamma_\mu \sin(ap_\mu) + m\mathbb{1} + \frac{1}{a}\mathbb{1}\sum_\mu (1 - \cos(ap_\mu)). \tag{2.45}$$

It can be seen from (2.45) that the Wilson term gives a contribution $2/a$ to the mass term for each momentum component that takes the value $p_\mu = \pi/a$. In the continuum limit the extra term from the fermionic

action (2.44) vanishes and the spurious quarks become infinitely heavy, therefore do not give contributions to the Green functions.

In our research we studied the lowest eigenmodes of the Dirac operator (discussed in chapter 3), since the localization phenomenon appears in that region. The behavior of the low end of the Dirac spectrum is sensitive to the chiral properties of the given lattice discretization, therefore we give special attention to the discretizations that have chiral symmetry on the lattice. For this let us take a glimpse at the continuum theory. The massless Lagrangian density has the symmetry $SU(N_f)_L \times SU(N_f)_R \times U(1)_V \times U(1)_A$, where N_f means the number of quark flavors, L and R refer transforming the left and right handed fermions independently and the V and A subscripts mean that the $U(1)$ transformations are performed separately on vectors and axial vectors. After quantization the $U(1)_A$ axial vector symmetry becomes explicitly broken, which is called the axial anomaly. The $SU(N_f)_L \times SU(N_f)_R$ part of the symmetry is spontaneously broken by the QCD vacuum to the subgroup of vector transformations $SU(N_f)_V$. These are the properties that need to be approached in a chirally symmetric lattice regularized theory.

In the following sections I will introduce two discretizations of the Dirac operator that we used in our studies. First the staggered Dirac operator, which besides the reduction of the number of the doublers to four, keeps a remnant chiral symmetry. Despite its drawbacks it is computationally very cheap and applicable to get a picture about what happens at the finite temperature transition of the quarks. Then I will show how to maintain exact chiral symmetry on the lattice and introduce a specific example, the overlap Dirac operator that satisfies this criterion.

2.3.1 Staggered discretization

The staggered discretization targets the doubling problem by distributing the Dirac degrees of freedom of fermions over the lattice points. More precisely we divide the lattice into the smallest possible hypercubes and for each hypercube we place a different spin components at its corners. With this construction the number of degrees of freedom is divided by four as we only keep one of the four Dirac components on a site. This effectively doubles the lattice spacing and the sine function

in (2.43) will have only one zero in the Brillouin zone for each of the different spin component staggered fermions. This way the discretized theory describes four degenerate quark species in the continuum as the quark propagator has only one pole in the Brillouin zone for each Dirac component that we distributed on the lattice.

For the mathematical construction of distributing the Dirac components of the quarks first consider the naively discretized Dirac operator of free fermions (2.38). It appears in the action in the following form

$$S_F = a^4 \sum_{n,m\in\Lambda} \bar{\psi}(n) D(m|n) \psi(m). \tag{2.46}$$

Then performing a local transformation of the variables

$$\begin{aligned} \psi(n) &\to S(n)\psi'(n) \\ \bar{\psi}(n) &\to \bar{\psi}'(n)S^\dagger(n) \end{aligned} \tag{2.47}$$

where $S(n)$ is a 4x4 unitary matrix, we can eliminate the Dirac components by making the Dirac operator diagonal in spin-space. With the choice, called the staggered transformation

$$S(n) = \gamma_1^{n_1}\gamma_2^{n_2}\gamma_3^{n_3}\gamma_4^{n_4}, \tag{2.48}$$

where $n_j, j = 1,2,3,4$ denote lattice indices, the mass term remains invariant, as the gamma matrices have the property of $\gamma_\mu^2 = \mathbb{1}$. Then we obtain

$$S^\dagger(n)\gamma_\mu S(n+\hat{\mu}) = \eta_\mu(n)\mathbb{1} \tag{2.49}$$

where we call $\eta_\mu(n) = (-1)^{n_1+n_2+\ldots+n_{\mu-1}}$ the staggered sign function. After the staggered transformation the gamma matrices are replaced by the 4x4 identity matrix multiplied by a sign factor $\eta_\mu(n)$. This means four identical components in the Dirac operator, from which we only keep one in the staggered action. The lattice fermionic action after the staggered transformation becomes

$$\begin{aligned} &a^4 \sum_{n,m\in\Lambda} \bar{\psi}'_i(n) D_S(n|m) \psi'_i(m) = \\ &= a^4 \sum_{n\in\Lambda} \bar{\psi}'_i(n) \sum_\mu \eta_\mu(n) \frac{\psi'_i(n+\hat{\mu}) - \psi'_i(n-\hat{\mu})}{2a} + m\psi'_i(n) \end{aligned} \tag{2.50}$$

where ψ'_i means the Dirac component we kept and D_S is the staggered Dirac operator. The interaction of the staggered fermions with

the gauge field appears simply through the link variables (discussed in section 2.2)

$$\begin{aligned} S_F^{stag} &= a^4 \sum_{n\in\Lambda} \bar{\psi}'_i(n) \sum_\mu \eta_\mu(n) \times \\ \times \frac{U_\mu(n)\psi'_i(n+\hat{\mu}) - U^\dagger_{-\mu}(n-\hat{\mu})\psi'_i(n-\hat{\mu})}{2a} &+ m\psi'_i(n). \end{aligned} \tag{2.51}$$

An important property of the staggered formulation is that it does not break explicitly the chiral symmetry of the massless action. One can see this by performing a chiral transformation on the staggered variables, where γ_5 is replaced by its staggered form (2.49)

$$\begin{aligned} \psi(n) &\to e^{i\alpha\eta_5(n)}\psi(n), \\ \bar{\psi}(n) &\to \bar{\psi}(n)e^{i\alpha\eta_5(n)}, \end{aligned} \tag{2.52}$$

where $\alpha \in \mathbb{R}$. By setting $m = 0$ the action (2.51) remains invariant under the transformation (2.52), which means the staggered action still maintains a global chiral symmetry.

Now let us consider the spectrum of the staggered Dirac operator

$$D_S(n|m) = \sum_\mu \eta_\mu \frac{U_\mu(n)\delta_{n+\hat{\mu},m} - U^\dagger_{-\mu}(n-\hat{\mu})\delta_{n-\hat{\mu},m}}{2a} + m\delta_{n,m}. \tag{2.53}$$

It can be shown that in the massless case D_S has the properties of anti-hermiticity and staggered γ_5-hermiticity

$$D_S(n|m) = -D_S^\dagger(n|m) \tag{2.54}$$

$$D_S^\dagger(n|m) = \eta_5 D_S(n|m)\eta_5 \tag{2.55}$$

where η_5 replaces $\gamma_5 = \gamma_1\gamma_2\gamma_3\gamma_4$ in the basis of the new staggered variables

$$\bar{\psi}(n)\gamma_5\psi(n) = \eta_5\bar{\psi}'(n)\mathbb{1}\psi'(n). \tag{2.56}$$

These two properties guarantee that the staggered eigenvalues λ_s come in complex conjugate pairs. This can be shown through the staggered Dirac operator's characteristic equation

$$\det(D_S - \lambda_s\mathbb{1}) = 0. \tag{2.57}$$

Multiplying the argument of the determinant by $\eta_5^2 = 1$ and using that D_S is staggered γ_5-hermitian one finds

$$\begin{aligned} \det(D_S^\dagger - \lambda_s \mathbb{1}) &= 0 \\ \det(D_S - \lambda_s^* \mathbb{1})^* &= 0 \end{aligned} \tag{2.58}$$

This means that λ_s and λ_s^* also satisfies the equation (2.57), thus the eigenvalue spectrum of D_S is purely real or consists of complex conjugate pairs. Using the property (2.54), we can conclude that it is the latter. The eigenvalues of D_S have zero real part and completely fall on the imaginary axis. With massive fermions ($m \neq 0$), the spectrum is shifted in the direction of the real axis by the mass parameter and the eigenvalues fall on a vertical line parallel to the imaginary axis as shown in Fig. 2.1.

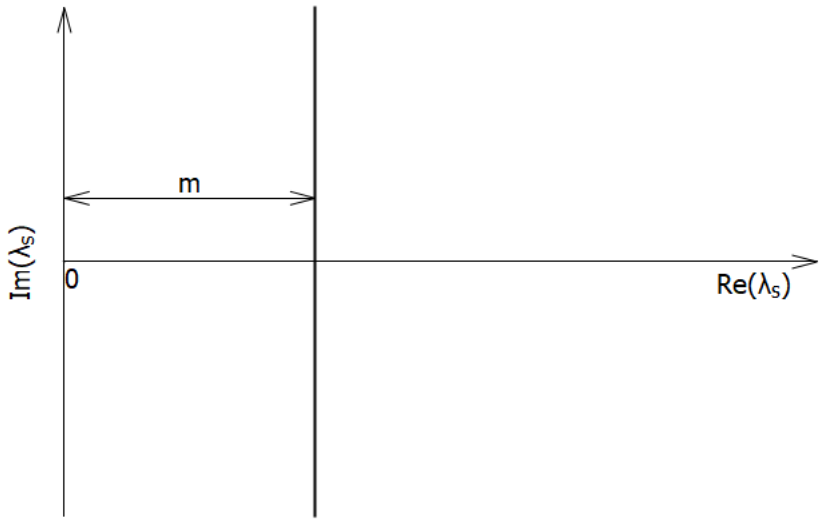

Figure 2.1: Eigenvalue spectrum of the staggered Dirac operator (bold line) with fermion mass m.

There is a procedure called gauge field smearing, generally used in lattice QCD, which improves the properties of lattice Dirac operators. This practically means that we replace the links of the lattice with a combination of the original and its neighboring links, in such a way that the new link will remain an element of the original gauge group. This smooths out the local fluctuations of the gauge field, which is beneficial in the case of the staggered Dirac operator as the different

quark components are affected by different gauge field links locally. In the case of staggered fermions we used the so called stout smearing [20], which is an analytical smearing method, therefore can be used in Monte Carlo simulations. In this case the generation of the new link happens as follows

$$U_\mu^{(n+1)} = e^{iQ_\mu^{(n)}} U_\mu^{(n)}, \tag{2.59}$$

where n is the number of smearing steps and Q_μ is a hermiatian, traceless matrix, which is constructed from the weighted sum of the products of perpendicular links neighboring the link intended to change. As $e^{iQ_\mu^{(n)}}$ is an element of the group SU(3) so is the new smeared link, therefore the transformation laws for the smeared links remains the same as in the case of the original links.

Staggered fermions are great candidates when one has to calculate the Dirac spectra of numerical simulations, because of the reduced number of degrees of freedom. Besides this, it has a remnant chiral symmetry, therefore spontaneous symmetry breaking can be detected by analyzing the eigenvalue spectrum (which can be done by using the Banks-Casher relation, discussed in section 3.4), as we study the finite temperature transition of the quarks. However, it does not have the full chiral symmetry of the continuum theory, therefore there still could be differences compared to real QCD. The lowest part of the Dirac spectrum is espically sensitive to the chiral properties of the discretization. This is the part of the spectrum that is involved in localization (our studies of the phenomenon of localization are presented in chapter 3), therefore in the next section I introduce how to create a Dirac operator that has exact chiral symmetry on the lattice.

2.3.2 Chiral symmetry on the lattice

First let us take a look at the chiral symmetry in continuum QCD. The massless fermionic action

$$S_F^{cont} = \int d^4x \; \bar{\psi}\gamma_\mu(\partial_\mu + iA_\mu)\psi = \int d^4x \; \bar{\psi} D^{cont} \psi, \tag{2.60}$$

where D^{cont} denotes the continuous Dirac operator. (2.60) is invariant when we perform chiral rotations on the fermion fields.

$$\begin{aligned} \psi &\to e^{i\alpha\gamma_5}\psi, \\ \bar{\psi} &\to \bar{\psi} e^{i\alpha\gamma_5}. \end{aligned} \tag{2.61}$$

The invariance of the action can be easily seen, if one inserts the transformed fields into (2.60). The invariance of S_F^{cont} can be expressed otherwise as the anti-commutation of D^{cont} with γ_5

$$D^{cont}\gamma_5 + \gamma_5 D^{cont} = 0. \tag{2.62}$$

With more than one massless quark flavors, S_F^{cont} is invariant under the generalized chiral transformations

$$\begin{aligned} \psi &\to e^{i\alpha\gamma_5 t_i}\psi, \\ \bar{\psi} &\to \bar{\psi}e^{i\alpha\gamma_5 t_i}, \end{aligned} \tag{2.63}$$

where the $N_f \times N_f$ matrices t_i $(i = 1, 2, ..., N_f^2 - 1)$ are the generators of rotations in flavor space.

Now it seems that we just have to find a lattice Dirac operator that satisfies equation (2.62) to make the lattice action exactly chirally symmetric. However, the so called Nielsen-Ninomiya theorem states that one cannot create a Dirac operator on the lattice that is local, does not produce doublers and also satisfies (2.62) at the same time. This problem was solved by Ginsparg and Wilson [21] by replacing the symmetry (2.62) with its lattice version

$$D\gamma_5 + \gamma_5 D = aD\gamma_5 D, \tag{2.64}$$

called the Ginsparg-Wilson equation. In the limit $a \to 0$, equation (2.64) produces the correct continuum form and it also makes it possible to define exact chiral symmetry for finite lattice spacing. Operators that satisfy the Ginsparg-Wilson equation, do not satisfy the locality criterion of the Nielsen-Ninomiya theorem [22]. This means they are not ultralocal, i.e. the distances of the interactions are not finite. However it is enough to require the matrix elements of the operators to fall exponentially with distance. By rearranging equation (2.64) we obtain

$$D\gamma_5(\mathbb{1} - \frac{a}{2}D) + (\mathbb{1} - \frac{a}{2}D)\gamma_5 D = 0. \tag{2.65}$$

Then we can define the lattice versions of the chiral rotations [23]

$$\begin{aligned} \psi &\to e^{i\alpha\gamma_5(\mathbb{1}-\frac{a}{2}D)}\psi, \\ \bar{\psi} &\to \bar{\psi}e^{i\alpha(\mathbb{1}-\frac{a}{2}D)\gamma_5}. \end{aligned} \tag{2.66}$$

The lattice action (2.46) for $m = 0$, stays invariant under such chiral transformations of the fermion fields if the Dirac operator satisfies

equation (2.65),

$$\begin{aligned} S_F &= a^4 \sum_{n,m\in\Lambda} \bar{\psi} e^{i\alpha(\mathbb{1}-\frac{a}{2}D)\gamma_5} D e^{i\alpha\gamma_5(\mathbb{1}-\frac{a}{2}D)}\psi = \\ &= a^4 \sum_{n,m\in\Lambda} \bar{\psi} e^{i\alpha(\mathbb{1}-\frac{a}{2}D)\gamma_5} e^{-i\alpha(\mathbb{1}-\frac{a}{2}D)\gamma_5} D\psi = \\ &= a^4 \sum_{n,m\in\Lambda} \bar{\psi} D\psi. \end{aligned} \tag{2.67}$$

Any Dirac operator which has the form

$$D = \frac{1}{a}(\mathbb{1} - M) \tag{2.68}$$

is a solution of the equation (2.64), as long as M is unitary and γ_5-hermitean matrix, i.e

$$M^\dagger M = \mathbb{1}, \quad M^\dagger = \gamma_5 M \gamma_5. \tag{2.69}$$

A more specific solution, the overlap operator, that is free of doublers, was presented by Neuberger [24, 25]. In the next section the overlap operator is discussed in more details.

2.3.3 Overlap discretization

The concrete form of Neuberger's solution of the Ginsparg-Wilson equation reads

$$D_{ov} = \frac{1}{a}(\mathbb{1} + A(A^\dagger A)^{-\frac{1}{2}}) \tag{2.70}$$

where A is constructed from a kernel Dirac operator, K, as

$$A = aK - \mathbb{1}. \tag{2.71}$$

The kernel is usually a Wilson-type Dirac operator, that is free of doublers. In this way we use a non-chiral Dirac operator as a kernel and construct a Dirac operator that is a solutions to the Ginsparg-Wilson equation (2.64). It yields a doubler free Dirac operator, which has an exact chiral symmetry also on the lattice. Let us choose the following form of the matrix A, which we also used in our research

$$A = aD_W - \mathbb{1}(M_0), \tag{2.72}$$

where D_W is the massless Wilson operator and M_0 is a real parameter of the kernel, with an absolute value close to one. Since in this case A is γ_5-hermitian, we can rewrite the product in (2.70) as $A^\dagger A = \gamma_5 A \gamma_5 A$. Then introducing the hermitian matrix $H \equiv \gamma_5 A$, the overlap operator can be written as follows

$$D_{ov} = \frac{1}{a}(\mathbb{1} + \gamma_5 H (H^2)^{-\frac{1}{2}}) = \frac{1}{a}(\mathbb{1} + \gamma_5 \mathrm{sgn}(H)), \tag{2.73}$$

where $\mathrm{sgn}(H)$ is the sign function.

As H is hermitian the spectral representation can be used for defining the sign function

$$\mathrm{sgn}(H) = \sum_i \mathrm{sgn}(\lambda_i) v_i v_i^\dagger. \tag{2.74}$$

In this case H is expressed in terms of an orthonormal eigenbasis, with corresponding eigenvalues denoted by λ_i and eigenvectors denoted by v_i. It was shown in section 2.3.1 that in the case of the staggered Dirac operator, γ_5-hermiticity leads to a spectrum that consists of complex conjugate pairs. Using the spectral representation (2.74) and multiplying the Ginsparg-Wilson equation (2.64) with $\gamma_5 v_i$ from the right and $v_i^\dagger \gamma_5$ from the left one obtains

$$\lambda_i^* + \lambda_i = a \lambda_i^* \lambda_i. \tag{2.75}$$

Expressing the eigenvalues explicitly with the sum of their real and imaginary parts $\lambda_i = x + iy$ (2.75) becomes

$$\left(x - \frac{1}{a}\right)^2 + y^2 = \frac{1}{a^2} \tag{2.76}$$

which is the equation of a circle centered at $1/a$ on the real axis. Hence we can conclude that the eigenvalues of the overlap Dirac operator fall on a circle in the complex plane as it is shown in figure 2.2. What the overlap construction did basically was projecting the eigenvalues of the kernel to a circle with radius $r = 1/a$. The circle intersects the real axis at 0 and $2/a$. If v_0 is a zero mode

$$D_{ov} v_0 = 0 \tag{2.77}$$

then using the Ginsparg-Wilson equation we get

$$\gamma_5 D_{ov} v_0 = D_{ov} \gamma_5 v_0 = 0. \tag{2.78}$$

This means D_{ov} commutes with γ_5 on the subspace of zero modes, therefore there exists a common eigenbasis. Thus we can chose v_0 to be an eigenvector of γ_5. In this case it has eigenvalues either $+1$ or -1 as $\gamma_5^2 = \mathbb{1}$, i.e. the zero modes of the overlap Dirac operator are chiral.

In our studies we were interested in the part of the spectrum near zero, because the localization of the quarks, which is discussed in details in chapter 3, affects the low end of the spectrum. As we move toward the continuum limit, the radius is increasing of the circle, on which the spectrum falls. Thus the eigenvalues in the vicinity of zero will fall on a vertical line and the doubler modes that have eigenvalues near $2/a$ will decouple, as they go toward infinity. Thus the overlap operator is a doubler free lattice Dirac operator and at the same time it has an exact chiral symmetry already for finite lattice spacing.

Even though the overlap operator has all these advantages, it is computationally demanding, because one has to calculate the sign function iteratively. Therefore we have to compromise between a faster calculation but giving up some of the properties of the continuum theory or using a chirally symmetric, doubler free operator at the expense of computer time.

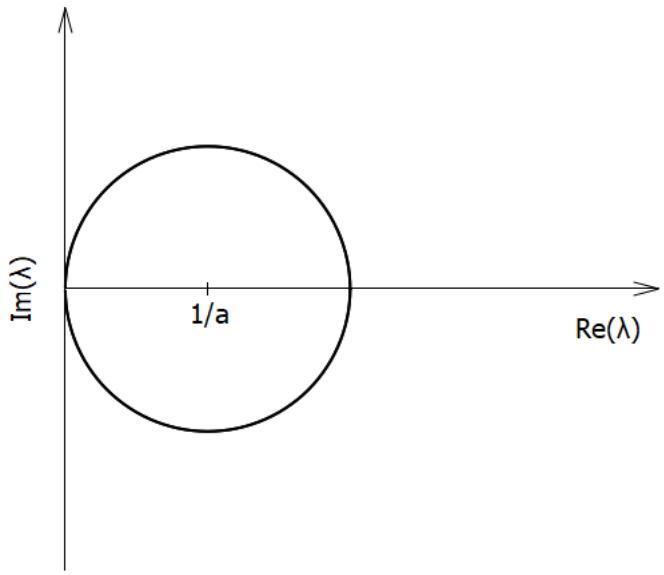

Figure 2.2: Eigenvalue spectrum of the overlap Dirac operator, that falls on a circle, whith radius $1/a$.

The overlap operator also can be improved by smearing the gauge links, similarly as in the case of staggered fermions (discussed in section 2.3.1). After smearing the overlap operator becomes more local [26] and besides that, the numerical calculation of the sign function will be faster also. For overlap fermions we used a different kind of smearing method, called hex smearing [27].

2.4 Finite temperature lattice QCD

In the present work we study the high temperature transition of the strongly interacting matter, therefore we have to simulate QCD at non-zero temperature. This section is dedicated to the theoretical discussion of how to introduce the temperature on the lattice and possibilities to study the transition of QCD matter.

As it was mentioned in section 2.1.1, there is a structural equivalence between the lattice formulation of the Euclidean path integral and a statistical mechanics system if we change the summation to an integral, i.e. changing from discrete to continuous variables. Then comparing the exponential factor in the partition function of a generic field ϕ on the lattice

$$Z = \int \mathcal{D}[\phi]\ e^{-S[\phi]}, \tag{2.79}$$

with the Boltzmann factor in the partition function of a statistical mechanical system

$$Z = \sum e^{-\beta H_{stat}}, \tag{2.80}$$

it can be seen, that the action of the field ϕ plays the role of the inverse temperature multiplied by the Hamiltonian function of the statistical system. Let us write out $S[\phi]$ in terms of the lattice discretized Lagrangian density

$$S[\phi] = a \sum_{n_4=0}^{N_\tau} a^3 \sum_{n_s} \mathcal{L}[\phi], \tag{2.81}$$

where n_4, n_s and N_τ denote respectively the lattice indices in time direction, the lattice indices in space directions and the temporal size of the system in lattice units. Then it can be seen, that simulations of lattices with finite temporal size $\beta \equiv aN_\tau$ is equivalent to simulations at finite temperature $\beta = 1/T$ (using the unit system $k_B = 1$), when the Lagrangian of the system is constant in time.

For a better illustration of the connection between the two theories, let us consider the partition function of a statistical quantum system

$$Z = \mathrm{tr}(e^{-\beta \hat{H}}) \tag{2.82}$$

where β is again the inverse temperature and $\hat{H}$ is the Hamiltonian operator of the system, that has a discrete spectrum. We arrive to a very similar formula by computing the transitional amplitude of a particle going from an initial position, x_i, to the same final position τ times later. After summing for all the possible positions one gets

$$\sum_i \left\langle x_i | e^{-\tau \hat{H}} | x_i \right\rangle = \mathrm{tr}(e^{-\tau \hat{H}}). \tag{2.83}$$

Here $e^{-\tau \hat{H}}$ is the time evolution operator in imaginary time τ. We can calculate the trace by the quantum mechanical path integral

$$\mathrm{tr}(e^{-\tau \hat{H}}) = \int \mathcal{D}x \; e^{-S}, \tag{2.84}$$

with the Euclidean action S on the right hand side. If we identify τ with β it can be seen that a system which is periodic in time is formally the same as a statistical system with finite β, i.e. finite temperature. Thus the partition function can be calculated by using the path integral formulation.

In lattice field theory we do the same, only changing the position variable to field variables and integrating over all possible field configurations after using lattice discretization as it was shown in section 2.1.1. This allows us to study lattice field theory, by using methods that are originally developed for statistical mechanical calculations. Now the period in time is the temporal extension of the lattice, aN_τ, and the continuum limit at finite temperature is taken by keeping

$$T = \frac{1}{aN_\tau} \tag{2.85}$$

fixed, while reducing a toward zero. This means when simulating a system at a given temperature we can refine the resolution of the lattice if we increase its temporal size.

The connection between finite temporal extension of the lattice and the temperature of the system can be seen intuitively if we analyze the frequencies of the eigenmodes, that can be created in such lattice. The boundary conditions in the time direction of bosonic (fermionic)

fields are periodic (anti-periodic). In this case the eigenvalue spectrum of the Dirac operator is discrete and (with trivial gauge background) the smallest eigenmode has a frequency of π/T for fermionic particles. Thus increasing the temperature, i.e reducing T will lead to higher frequency and thus higher energy eigenmodes, which is the expected behavior when heating the system.

After introducing finite temperature on the lattice we can move to discuss the finite temperature transition of the strongly interacting matter. For this let us look at the case of pure gauge theory, that we simulated in our studies (discussed in chapter 3). There is a lattice observable, called the Polyakov loop, which we build up by taking the trace of the product of the gauge link variables (gauge field variables)

$$P(n) = \mathrm{tr} \left(\prod_{n_4=0}^{N_\tau - 1} U_4(n, n_4) \right) \tag{2.86}$$

The spatial lattice index is denoted by n and the lattice index in the time direction is denoted by n_4. $P(n)$ is a closed loop due to the periodic boundary conditions, therefore it is gauge invariant (gauge invariance of closed loops is discussed in section 2.2). The Polyakov loop is an important observable when one studies the deconfining transition of the quarks. It serves as an order parameter of color confinement, which I will show in the following.

It can be shown that the average of the Polyakov loop is related to free energy of a system with one static quark (i.e. an infinitely heavy quark) relative to the free energy without the presence of the static quark

$$\left\langle \frac{1}{N_c} \sum_{n \in \Lambda} P(n) \right\rangle = e^{-\beta F_q}, \tag{2.87}$$

where $\langle . \rangle$ is the average with respect to the path integral, N_c is the number of the lattice points in one timeslice, β is the inverse temperature and F_q is the free energy (measured in lattice units) of a static quark, relative to the vacuum. The correlator of two oppositely oriented polyakov loops located at spatial lattice sites n and m

$$\left\langle P(n) P^\dagger(m) \right\rangle = e^{-\beta F_{q\bar{q}}(n,m)} \tag{2.88}$$

gives the free energy $F_{q\bar{q}}(n, m)$ of a static quark-antiquark pair separated by the distance $|m - n|$. In the limit of infinite spatial separation

we obtain

$$\lim_{|m-n|\to\infty} \left\langle P(n)P^{\dagger}(m) \right\rangle = |\left\langle P \right\rangle|^2, \tag{2.89}$$

where we introduced the notation $P \equiv \sum_{n\in\Lambda} P(n)$ for the spatial average of the Polyakov loop. It can be seen from (2.89), that when $\langle P \rangle$ is equal to zero, that means $F_{q\bar{q}}(n,m)$ goes to infinity as the distance is increased between the quark-antiquark pair. If $\langle P \rangle$ differs from zero, then the free energy between the quark-antiquark pair separated by a large distance goes toward a finite constant value. This means that, there is the following relationship between the average of the Polyakov loop and color confinement

$$\begin{aligned} \langle P \rangle = 0 \quad &\rightarrow \quad \text{confinement} \\ \langle P \rangle \neq 0 \quad &\rightarrow \quad \text{deconfinement.} \end{aligned} \tag{2.90}$$

Considering equation (2.87), it can be seen that if quarks are confined the left hand side of (2.87) is zero. This means that the free energy of a static heavy quark is infinitely large, therefore we cannot observe free quarks. In contrast, when one considers deconfinement, the expectation value of the Polyakov loop is nonzero and the free energy is finite. This means that by observing the Polyakov loop in lattice calculations one can detect the transition from the low temperature phase of color confinement, where quarks only appear bound to each other, forming color neutral hadrons, to the high temperature state where hadronic borders are blurred and the quarks and gluons form a quark-gluon plasma.

The quenched action is invariant under the so called center transformation. This means the transformation of all of the temporal link variables at a given time slice, with a center element, C, of the group $SU(3)$

$$\begin{aligned} U_4(n,n_4) &\to CU_4(n,n_4), \\ C &\in [\mathbb{1}, \mathbb{1}e^{i\frac{2}{3}\pi}, \mathbb{1}e^{-i\frac{2}{3}\pi}]. \end{aligned} \tag{2.91}$$

As C is an element of the gauge group it satisfies the property

$$CC^{\dagger} = \mathbb{1}. \tag{2.92}$$

The gauge action remains invariant under such transformation, because it is constructed from the trace of closed loops not wrapping around the system in the temporal direction. Therefore the loops have as many elements pointing in one temporal direction as in the opposite direction

and the center elements commute with all of the gauge group elements. However, the Polyakov loop is not invariant, because it is closed in a nontrivial way and it is constructed from temporal link variables that are pointing in only one direction. The expectation value of the Polyakov loop on an ensemble of configurations changes as

$$\langle P \rangle \to e^{i\frac{2k}{3}\pi} \langle P \rangle ; \quad k = 0, 1, 2 \ , \tag{2.93}$$

after center transformation. If the system is confined the averaged Polyakov loop vanishes $\langle P \rangle = 0$, therefore the expectation value remains the same. In the deconfined state the expectation value of P is non-zero, which leads to the spontaneous breaking of the center symmetry. This makes the Polyakov loop the order parameter of deconfinement. Since the action and the group measure are invariant under center transformations, there are three sectors of the Polyakov loop that have the same statistical weight, each belonging to the center transformed value of P. In the thermodynamic limit the spontaneous breaking of the center symmetry is exact, similarly as in spin systems without an external magnetic field. However, with dynamical fermions, the fermion determinant in the path integral breaks the center symmetry explicitly and the volume averaged value of the Polyakov loop stays in the real sector. Therefore in lattice calculations we are interested in the real Polyakov loop sector, for which we can assign a physical meaning.

The spontaneous breaking of center symmetry signals the deconfining transition, which is a genuine first order phase transition [28] in quenched QCD (the limit of infinite quark masses). In contrast, in full QCD, with physical quark masses, deconfinement is only a crossover. The nature of the finite temperature transition as a function of the quark masses is shown in Fig 2.3. On the left hand side sketch the quenched theory is in the upper right corner of the plot. With finite but large quark masses the transition remains first order around the quenched point. At the opposite corner, there is another area where the chiral transition is expected to be a genuine first order phase transition, around the chiral limit (the limit of zero quark masses). On the boundary lines of the first order regions the transition is second order and between them there is a crossover region of hadron gas changing to quark-gluon plasma. With our recent knowledge the finite temperature transition with physical quark masses is a rapid crossover [1], as the physical point is near the first order region of the plot (shown in figure 2.3a). On the righ hand side sketch the transition line is shown

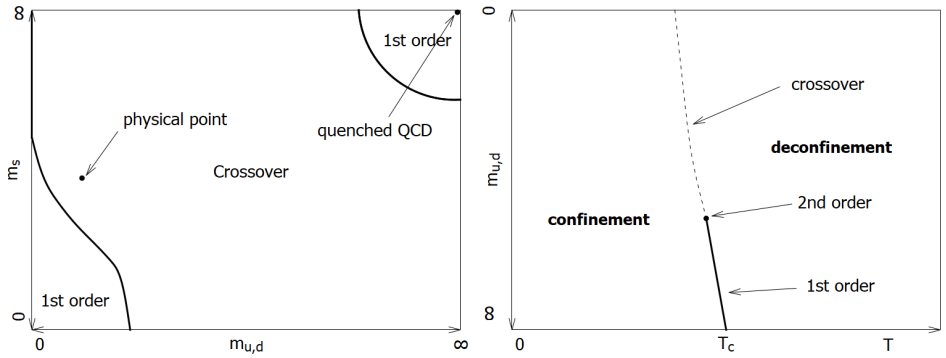

(a) (b)

Figure 2.3: (a) Cross section of the three flavor phase diagram at the up/down degenerate quark mass ($m_{u,d}$) - strange quark mass (m_s) plane of the deconfining transition at the transition temperature. At the counter line of the first order area at right upper corner the transition is second order. (b) QCD phase diagram with two flavors at $\mu = 0$. T_c is the critical temperature of the deconfining transition at the quenched point. The endpoint of the first order line is a second order phase transition point.

between the two states of the quarks, with two degenerate quark flavors on the vertical axis and the temperature on the horizontal axis. The transition line corresponds to the upper boundary of figure 2.3a, where the mass of the third quark is infinite and thus decouples from the theory. Starting from the quenched point on figure 2.3b the transition becomes weaker as the quark mass decreases. The first order line ends in a second order transition point and continues as a crossover line. There is a smooth connection among the different regions of this line and the transition is basically the same for all values of the mass parameter, only its strength changes. Simulations of pure gauge theory, therefore give the possibility to gain information about the nature of the finite temperature transition of the strongly interacting matter in a computationally more economic way than with dynamical quarks.

Chapter 3

Localization

3.1 Anderson localization

Anderson localization is the phenomenon in condensed matter physics, when quantum particles become localized in the presence of a disorder in the system. This happens due to wave interferences, which hinder the diffusion of particles in the disordered medium. The states at a given energy are either localized or extended depending on the degree of the disorder. There exist critical energy values which divide the energy spectrum into regions in which all states are either localized or delocalized. A critical energy value which separates the localized states from the extended states is called the mobility edge. In electronic systems, if the mobility edge is above the Fermi energy, localization suppresses the movement of electrons in the medium. In the localized region the electronic eigenstates ψ of the Hamiltonian decay exponentially with distance

$$|\psi^2(r)| \sim e^{-\frac{|r-r_0|}{\xi}}, \tag{3.1}$$

where ξ is the localization length and r_0 is the position where the wave function is localized. If the disorder reaches a strength, where all electronic states are localized, the electric conductivity of the system becomes zero, hence the medium becomes an insulator. Thus there exists a disorder induced transition from metallic phase (extended states in the conduction band) to insulator phase (only localized states at the conduction band) as the strength of the disorder is varied. This metal-insulator transition is called the Anderson transition and it was shown to be a second-order phase transition [29]. Nowdays we use this name in a broader sense including many other phenomena, where the transition between localized and extended states happens, not just in the

case of a metal-insulator transition.

Since the Anderson transition is second order, the critical behavior is scale independent and we can distinguish different universality classes, that only depend on a few parameters of the system (eg. dimension and symmetries). The first classification of disordered systems by their critical behavior comes from Dyson by further developing Wigner's random matrix theory. There are three so called Wigner-Dyson classes for ensembles of Hamiltonians the entries of which are random numbers following a given statistical distribution. The Anderson model describes such Hamiltonian of disordered systems, which in the simplest case, when only nearest neighbor interactions are involved, is the following [30]

$$H = V \sum_{n\in\Lambda,\mu} |n\rangle\langle n+\hat{\mu}| + \sum_{n\in\Lambda} \epsilon_n |n\rangle\langle n|. \tag{3.2}$$

The first term is a delocalizig hopping term between the states $|n\rangle$and$\langle n+\hat{\mu}|$ on lattice sites n and its nearest neighbor site $n+\hat{\mu}$ and ϵ_n is a random localizing potential.

The three Wigner-Dyson universality classes of disordered systems are the following [30–32].

- The Hamiltonian is a real symmetric matrix $H = H^T$. In this case V and ϵ_n are real numbers, thus the eigenvalues of H are invariant with respect to orthogonal transformations. The set of such Hamiltonians belongs to the orthogonal symmetry class.

- The Hamiltonian is a complex Hermitian matrix $H = H^\dagger$. In this case V is a complex number and the set of this kind of matrices is invariant under unitary transformations. Therefore H belongs to the unitary symmetry class.

- The third symmetry class is the symplectic class. Hamiltonians belonging to this class are self-dual Hermitian matrices, i.e. they can be divided into quaternionic 2×2 blocks. In this case H can be written in terms of the Pauli matrices $\sigma_j, j = 1,2,3$

$$H^s_{nm}\mathbb{1}_2 - i\sum_j H^a_{nm}\sigma_j, \tag{3.3}$$

  where $\mathbb{1}_2$ is the 2×2 unit matrix, H^s_{nm} is real symmetric and H^a_{nm} is real antisymmetric. The set of such matrices is invariant under the transformations of the symplectic group.

The probability distribution of the entries of these random Hamiltonians remain invariant under the above mentioned three transformations, respectively. Therefore, H and its transform H' will have the same contribution for the partition function. That is the reason why they can be classified into symmetry classes.

In finite temperature QCD the quarks also undergo an Anderson-type localization. When this occurs, localized quark modes appear at the low end of the Dirac spectrum, which they occupy up to the mobility edge. Above the mobility edge all of the eigenmodes of the Dirac operator are extended spatially. The difference from condensed matter physics is that the physical quantities depend on the whole Dirac spectrum and we cannot focus only on one part of the spectrum when we are calculating observables. Therefore we cannot track the transition from localized to extended modes in this way. The transition in the spectrum of the Dirac operator is also a second order transition, the critical point of which is the mobility edge. It was demonstrated in a scaling study [33], that the QCD transition in the spectrum is an Anderson-type transition by showing that the critical exponent for the correlation length is consistent with that of the three dimensional Anderson model of unitary class. In this work we study the finite temperature transition of QCD and the phenomenon of quark localization which is shown in details in the following sections.

3.2 Localization with Staggered fermions

A brief summary of the phenomenon of localization was given in the previous section. We studied the localization of the strongly interacting matter, that happens during the crossover, when quarks go from a hadronic state to quark-gluon plasma (QGP). At the low temperature phase the quarks are in a bound state forming hadrons due to color confinement. In the QGP phase the boundaries of hadrons are blurred and quarks and gluons form a state, where they are liberated from color confinement and free color charges can be observed. In this high temperature phase quarks become deconfined, therefore the transition to QGP is called deconfinement. In full QCD, i.e. in the physical point with physical quark masses, deconfinement happens smoothly (i.e. it is a crossover) and it is accompanied by two other phenomena. These phenomena are the approximate restoration of the spontaneously bro-

ken chiral symmetry[1] and the spatial localization of the quark modes with the lowest Dirac eigenvalues. During our research we investigated the latter. Our main goal was to understand the connection among the phenomena that happen in the crossover region.

We wanted to find the temperature where localization occurs, i.e. the temperature where the first localized quark modes appear. At the low temperature regime, where quarks are bound into hadrons, all the modes are extended in space [34]. Then moving upward to the crossover region, at a certain temperature localized modes appear in the spectrum of the QCD Dirac operator. The localized modes occupy the low end of the Dirac spectrum up to the mobility edge, while above that the rest of the spectrum consists of extended modes. This behavior of the quark modes in the spectrum is the same as the transition in Anderson-type models. By turning the approach around, going from the high temperature phase toward the crossover, the region in the spectrum which is occupied by localized quark modes becomes smaller, as it is illustrated in Figure 3.1, and somewhere in the crossover region the localized modes disappear. In the figure we show a sketch of the spectral density at the high temperature phase, where chiral symmetry is restored. In this case the spectrum is depleted around the origin, which is connected to chiral restoration through the Banks-Casher relation, discussed in section 3.4. The mobility edge shrinks as the temperature decreased and at a well defined temperature, at the critical temperature of localization, it becomes zero. Meanwhile, the deconfining transition does not have a precise critical temperature, as it is only a crossover.

Localization happens at the same temperature region as deconfinement, therefore the question arises whether one of the phenomena is driven by the other, or the transitions only happen close to each other but do not exactly coincide. In full QCD, we cannot associate an exact critical temperature with deconfinement, however, there are models similar to QCD, where it is a first order phase transition (the phase structure of QCD depending on the quark masses is shown in Figure 2.3, in section 2.4). This is the case in the limit of large quark masses, i.e. the quenched approximation of QCD (discussed in Section 2.2.1). The critical temperature of deconfinement is determined in the quenched theory in Ref. [28]. To understand the connection between the deconfining transition and localization, our main goal was to compare the

[1]The exact chiral symmetry is broken by the nonzero masses of the quarks.

critical temperatures of the two phenomena. The temperature where the localization happens in the quenched theory was not known before, therefore it was our task to determine it. The process of determination of the critical temperature is discussed in details in the following sections.

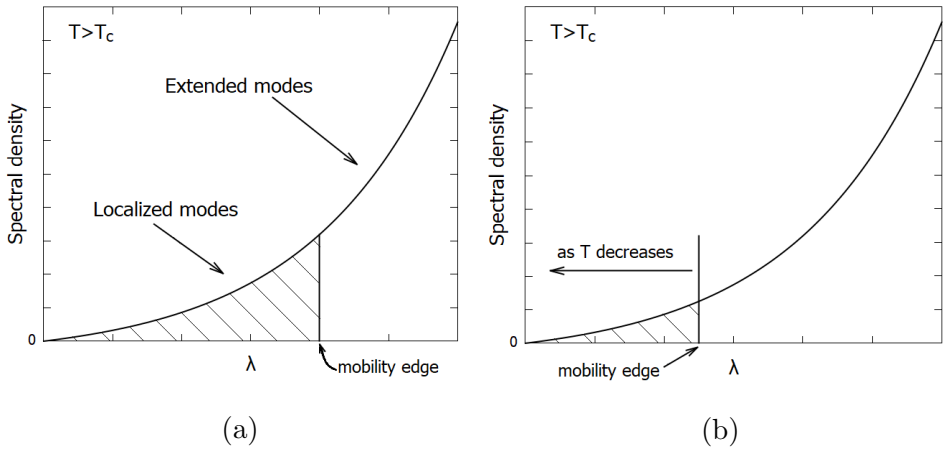

(a) (b)

Figure 3.1: Sketch of the spectral density above the the critical temperature of localization. Figure (a) shows a higher temperature state than figure (b). The dashed area illustrates the localized part of the spectrum. If the temperature is lowered toward the critical temperature the localized modes occupy a smaller part of the spectrum, as it is shown in figure (b).

3.2.1 Simulation details

We simulated pure SU(3) gauge theory, i.e. the quenched approximation of QCD, on a hypercubic lattice. This was done by the Monte Carlo method using the Wilson gauge action (2.14). We wanted to know whether deconfinement and the appearance of the first localized modes occur at compatible temperatures. To this end we kept the temporal size in lattice units fixed in the simulation and set the temperature with the inverse gauge coupling β of the Wilson action, which can be done because we can parametrize the state of the system either by the temperature or the gauge coupling in the simulation. We chose to use β, because strictly speaking, it is not possible to set a physical scale for the temperature in the quenched theory, as the quark masses are not the physical ones. Besides that, the temperature is an increasing function of β, therefore it is more illustrative to use this value than the

gauge coupling itself. Therefore to know whether the critical temperature of the two phenomena coincide, we had to compare the critical inverse gauge coupling for localization β_c^{loc} with that of deconfinement β_c^{deconf}. For a better transparency and to give some technical details I give a schematic description of the procedure as follows.

We generated gauge field configurations at several different gauge couplings above the deconfining critical point, i.e. simulated the behavior of the gauge field at different temperatures at the QGP phase. To calculate the mobility edge we needed to determine the low part of the eigenvalue spectra of the Dirac operator on each gauge field background. We determined as many eigenvalues as were needed to capture the transition from localized to extended modes in the spectra. We used stout smearing (discussed at the end of section 2.3.3) on the gauge links, with smearing parameter $\rho = 0.15$ [35]. The smearing procedure was done two times and we calculated the low eigenvalues of the massless staggered Dirac operator (2.53), by using the Krylov-Schur algorithm [36] on the smeared gauge configurations. As the spectrum of the staggered operator, in this case, is purely imaginary and symmetric around zero (see section 2.3.1), we only computed the positive half of the spectrum.

After we gathered data from the simulation, we started the statistical analysis of the eigenvalues. We determined the mobility edge from the ensemble of eigenvalue spectra corresponding to each β (discussed in the following section). To determine β_c^{loc} we had to find the coupling where the mobility edge disappears. For this we had to go close to the critical coupling but could not go arbitrary close, because we experienced during our calculations, that the correlation length of the gauge fluctuation increased toward the critical point of deconfinement. To compensate for this we needed lattices with larger spatial volume as we went toward the critical coupling. The linear sizes of the lattices at different values of β are gathered in Table 3.1. We determined the mobility edge as a function of the inverse gauge coupling and extrapolated the critical value where the mobility edge disappeared. A detailed discussion of this is given in section 3.2.3.

The above described procedure was done for three different temporal extents $N_t = 4, 6$ and 8 in lattice units, which correspond to three different resolutions of the lattices (the connection between the lattice

spacing and the temporal size of the lattice is discussed in section 2.4). The details of the simulation for different temporal sizes can be seen in Table 3.1. After this we could compare our results of β_c^{loc} with β_c^{deconf} for the different lattice spacings and we were able to draw conclusions about the continuum from these results. The procedure of the determination of β_c^{loc} was as follows.

- Generating gaue field configurations.
- Calculating the lowest eigenvalues of the staggered Dirac spectra for each configuration.
- Calculating the mobility edge from the spectra at different gauge couplings.
- Determining the critical coupling where the mobility edge disappears by extrapolation.
- Repeating the points above with finer resolution lattices.

We used previously written codes for the generation of gauge field configurations with the Monte Carlo method and for smearing and calculating the eigenvalues and some other observables (for example the spatial average of the Polyakov loop). We chose the gauge coupling values where the simulations were done and used the local computer network in the Institute for Nuclear Research of the Hungarian Academy of Sciences for running the simulations. The eigenvalues were calculated by parallel computing using several NVIDIA GeForce 670 and NVIDIA GeForce 770 type graphic cards connected to each other. For the statistical analysis of these data and the calculation of the critical coupling of localization I used my own code written in C++.

We used those eigenvalue spectra for the calculations that were in the real Polyakov loop sector. The reason for this is that the real Polyakov loop sector is the one where the system stays, when simulating with finite quark masses, i.e. it is the physical sector. In figure 3.2a is shown a typical scatter plot of the Polyakov loop sectors in the complex plain, obtained from simuations when tunneling between the sectors could occur. The dots in the figure represent the spatial average of the Polyakov loop in a gauge configuration. When tunneling occurs between the different Polyakov loop sectors, the average value of P changes smoothly and prefers to stay in one of the sectors longer, than

N_t	4			6				8			
β	N_s	N_{cf}	N_{ev}	β	N_s	N_{cf}	N_{ev}	β	N_s	N_{cf}	N_{ev}
5.693	32	1061	600	5.897	32	532	900	6.08	56	306	600
	40	1192	1100		40	1249	1000		64	538	400
	48	2381	1500		48	682	1350	6.1	48	439	500
5.694	32	1715	600	5.9	32	998	900		56	681	600
	40	1005	1100		40	925	1000		64	486	400
	48	2014	1600		48	813	1350	6.15	48	781	500
5.695	32	2184	650	5.91	32	1068	900		56	698	600
	40	2012	1100		40	834	1000		64	385	400
	48	2028	1300		48	1088	1350	6.18	48	636	500
5.696	32	1073	900	5.92	32	1822	600		56	964	600
	40	1628	1000		40	960	1000		64	384	400
5.6975	32	2291	600	5.93	32	806	900	6.2	48	675	500
	40	1524	1100		40	1050	1000		56	778	600
	48	2000	1500	5.94	40	1092	1000		64	418	400
5.6985	40	1973	1000	5.95	32	562	600	6.25	48	758	500
5.7	24	4139	600		40	1276	1000		56	652	600
	32	4040	800	5.96	32	832	1000		64	320	400
	40	1022	1000		40	1032	1000	6.3	48	578	500
5.71	24	2509	300	5.95	32	562	600		56	616	600
	32	2507	450		40	1276	1000		64	452	400
	40	1073	1100	6.0	32	1392	900				
5.74	24	2024	300		40	1958	1000				
	32	2501	450								
	40	2390	1100								

Table 3.1: Parameters of the simulation for temporal sizes (N_t) 4,6 and 8 shown in different columns. In each column the Wilson plaquette gauge couplings (β), the size of the lattice in spatial direction (N_s), the number of the configurations (N_{cf}) and the number of eigenvalues computed for each configuration (N_{ev}) are listed.

between them. Therefore less configurations have an average Polyakov loop value that do not belong to one of the sectors than those which belong to one. Thus we could separate those configurations, which had an average P of the real sector by checking the density of the configurations of the real part of P, as we are interested in the real sector. We accepted those configurations to belong to the real sector that were above the minimum between the two peeks of the density function, which can be seen in figure 3.2b.

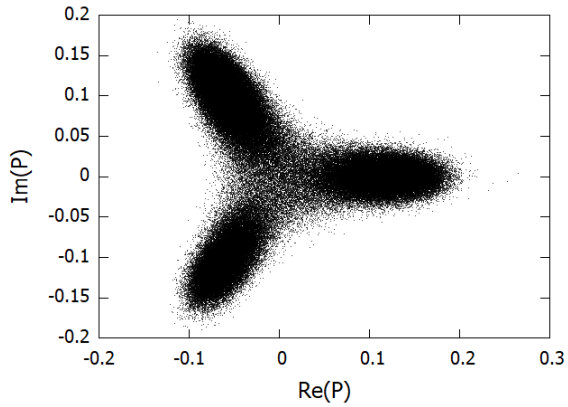

(a)

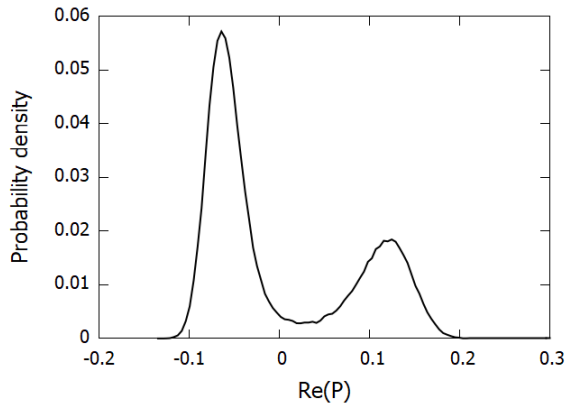

(b)

Figure 3.2: Figure (a) shows the complex value of the averaged Polyakov loop on different gauge configurations. Each dot corresponds to one configuration of the gauge field. Figure (b) shows the distribution of the real part of the spatially averaged Polyakov loop for all of the configurations shown in figure (a).

In the following sections I give a detailed discussion about the work I have done following the configuration generation and the determination of the low end of the Dirac spectra.

3.2.2 Mobility edge

Starting from the QGP phase and going toward lower temperatures, localized quark modes fill up smaller and smaller parts of the Dirac spectrum and at a certain critical temperature they completely disappear and all of the modes become delocalized. We wanted to find this critical temperate, or in the quenched theory, which we used in our simulations, the critical gauge coupling of localization. For this we tracked the change of the boundary between the localized and extended modes in the spectrum, i.e. the mobility edge λ_c, as a function of β. Thus we had to find the critical value where the mobility edge becomes zero

$$\lambda_c(\beta_c^{loc}) = 0. \tag{3.4}$$

This gives the critical gauge coupling for localization, which we can compare to the quenched value of the critical coupling corresponding to deconfinement. In this section I present the details of how we determined the mobility edge from the eigenvalue spectra of the staggered Dirac operator, which was a pivotal point during our investigation.

First we had to find out whether eigenmodes are localized or extended at a given part of the spectrum. A simple way to do this was to analyze the statistics of the level spacings s, i.e. the differences between the nearest neighbor eigenvalues. There are known universal results for the distribution of s from random matrix theory. To uncover this, first we have to remove the system specific scale from the eigenvalue spectra to reveal universal properties. For this we needed to rescale the eigenvalues in order to make the spectral density and therefore s system independent. To this end we used the so called unfolding procedure, which means rescaling the eigenvalues so that the spectral density will be set to unity throughout the whole spectrum. Then we calculated s from the unfolded Dirac spectra. After unfolding the average level spacing will be unity too and we can write s in terms of the neighboring eigenvalue differences $\Delta\lambda$ as $s = \Delta\lambda / \langle \Delta\lambda \rangle$.

Technically unfolding can be performed in different ways that are equivalent if the spectrum is dense enough. In our case it was simply done by arranging the eigenvalues in ascending order and labeling them

by their rank, normalized with the number of configurations. By doing this the spacing between the neighboring unfolded eigenvalues in the whole spectrum will be the inverse of the number of configurations. Therefore the average spacing of the eigenvalues per configuration will be unity, just like the average spectral density. In this way the characteristic scale of the system has been removed and universal spectral fluctuations can be studied. In random matrix theory these fluctuations were studied and analytic results are known for the unfolded level spacing distribution (ULSD) [37].

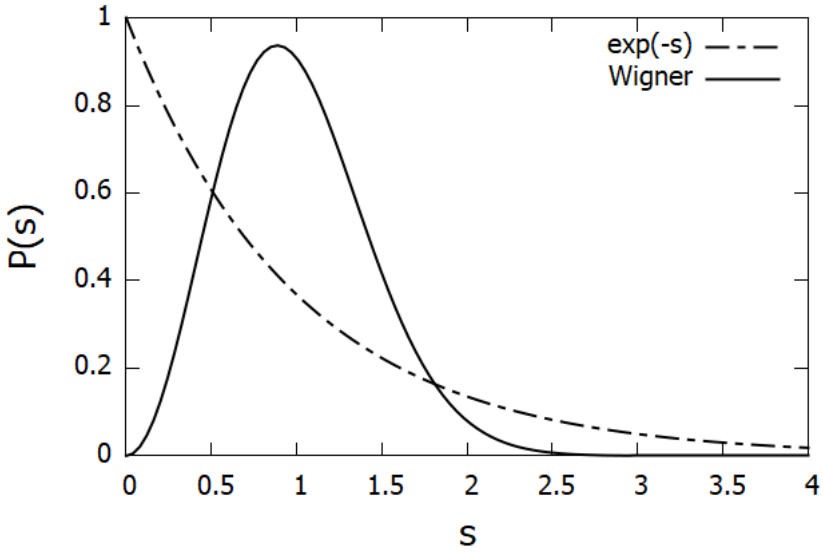

Figure 3.3: Probability density functions of the level spacings for Poisson distribution (dashed line) and the Wigner surmise (continuous line).

Unfolded level spacings obey different distributions for extended and localized modes, which makes it possible to distinguish between the two cases and tell whether quark modes are localized or not in a given part of the spectrum. Localized modes do not interact with each other, therefore the eigenvalues distribute independently. The eigenvalues in this case obey Poisson distribution and the level spacing density function is the following

$$P(s) = \exp(-s). \tag{3.5}$$

In contrast, extended modes are mixed by the gauge field and their level spacing distribution can be approximated by the so called Wigner

surmise. It is different for the three cases of the Wigner-Dyson universality classes (these are discussed in section 3.1). In the case of the unitary class to which the staggered Dirac operator belongs, the density function of the level spacings is the following

$$P(s) = \frac{32}{\pi^2} s^2 \exp(-\frac{4}{\pi} s^2). \tag{3.6}$$

The density functions in the two cases are demonstrated in figure 3.3.

We tracked the ULSD through the spectrum so that we could find where the transition from localized to extended modes happens in the spectrum. We did this by dividing the Dirac spectrum into small bins and determined the statistics of the level spacings in each bin. A simple way to detect the change in the statistics is to calculate a parameter of the distributions and plot it as a function of eigenvalues λ. The parameter we used was the integrated probability density function

$$I_{s_0} = \int_0^{s_0} P(s) ds, \tag{3.7}$$

where the upper limit of the integral, s_0, is a parameter that can be arbitrarily chosen. We get the greatest difference between the values of I_{s_0} corresponding to localized and extended modes if we choose the upper limit to be the first intersection point $s_0 = 0.508$ of the two probability density functions. Areas of the probability density functions calculated by the integral for this case are shown in figure 3.4.

After fixing the upper limit of the integral at the first intersection point of the two densities, we could track the changing of the integrated probability density function through the spectrum. We denote the integral with the fixed upper limit as $I_{0.5}(\lambda)$ from now on. The values of this quantity at the two limiting distributions are $I_{0.5}^{\mathrm{P}} = 0.398$ and $I_{0.5}^{\mathrm{W}} = 0.117$, for Poisson distribution corresponding to localized modes and for the Wigner surmise, that describes the extended modes, respectively. The change of $I_{0.5}(\lambda)$ through the spectrum is illustrated on figure 3.6a with a typical graph for lattices with temporal extent $N_t = 4$. On all the figures dimensionless quantities are shown, i.e. the eigenvalues are indicated in lattice units $a\lambda$. The data show that the function changes smoothly between $I_{0.5}^{\mathrm{P}}$ and $I_{0.5}^{\mathrm{W}}$.

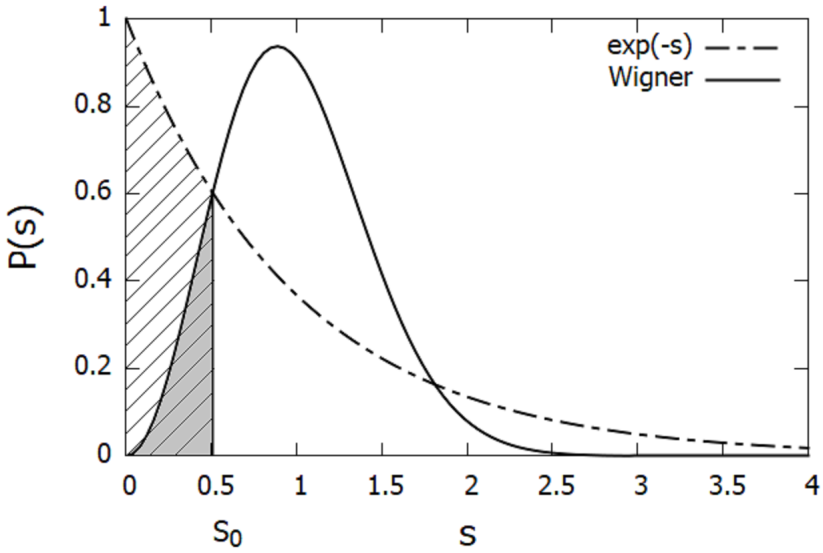

Figure 3.4: The integrated areas are shown up to the first intersection point $s_0 = 0.508$ of the Poisson and Wigner surmise density functions. The dashed area and the shaded area correspond to $I^P_{0.5}$ and $I^W_{0.5}$ respectively.

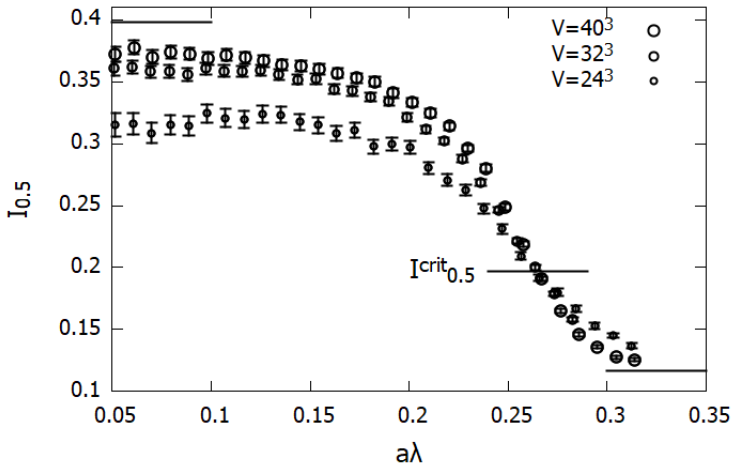

Figure 3.5: The integrated probability density function at inverse gauge coupling $\beta = 5.71$ and $N_t = 4$ for three different spatial volumes. Larger dot sizes sign larger volumes.

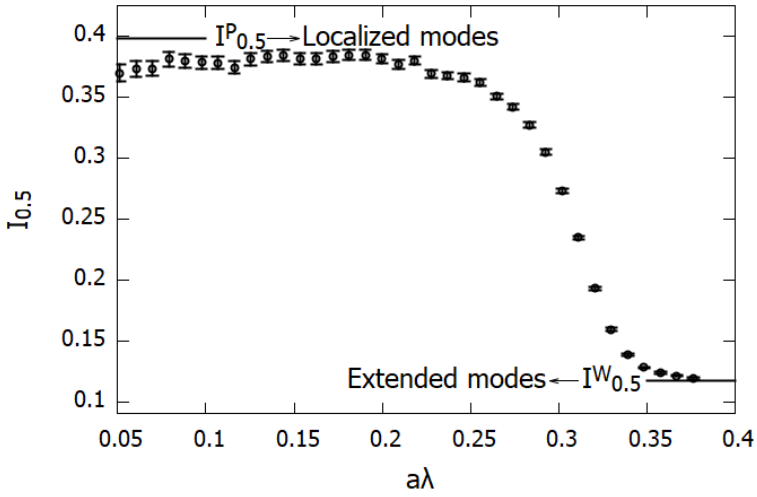

(a) : The integrated probability density as a function of the eigenvalues (λ) calculated from lattices with temporal extent $N_t = 4$ and spatial volume $V = 40^3$ at inverse gauge coupling $\beta = 5.74$. The two lines show the value of the function for the two limiting distributions corresponding to localized and extended modes.

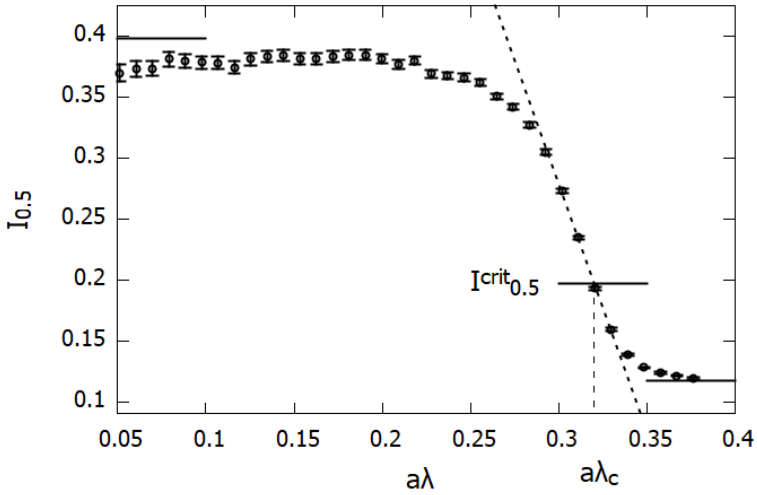

(b) : Determination of the mobility edge (λ_c). Linear fit (densely dashed line) on the integrated probability density function around its critical value (middle horizontal line). λ_c is where the linear fit reaches the critical value of $I_{0.5}(\lambda)$.

Figure 3.6

In the thermodynamic limit, i.e. at infinite spatial volume, the

transition from $I_{0.5}^{\mathrm{P}}$ to $I_{0.5}^{W}$ is infinitely steep, since it is a transition of second order (discussed in Ref. [33]). Its critical point is the mobility edge λ_c, which is unambiguously defined in this case. However, we work with lattices that have a finite spatial volume, which induces the occurrence of finite size effects. In this case, there is an ambiguity in how we define λ_c. In fact, we can define the mobility edge in a finite lattice by any value that satisfies $I_{0.5}(\lambda_c) = C$ where $C \in (I_{0.5}^{\mathrm{P}}, I_{0.5}^{\mathrm{W}})$ is a constant. Going toward the thermodynamic limit, any λ_c defined in this way would converge to the correct value corresponding to the infinite volume limit. However, it is optimal to choose a value which has small finite size deviation from the the critical point calculated in the infinite volume limit. Therefore we chose λ_c to be the value corresponding to the critical distribution $I_{0.5}^{crit}$ between the Poisson distribution and the Wigner surmise, which was determined in a finite size scaling study [38]. I.e. identified λ_c with the value where the integrated probability density function reaches its value for the critical distribution $I_{0.5}^{crit} = 0.1966$. It can be seen on figure 3.6b that this value is in the vicinity of the inflection point of the function $I_{0.5}(\lambda)$, therefore it can be approximated with a linear function $I_{0.5}^{lin}(\lambda)$ around the critical point. In this way λ_c can be easily determined by solving the equation $I_{0.5}^{lin}(\lambda_c) = I_{0.5}^{crit}$.

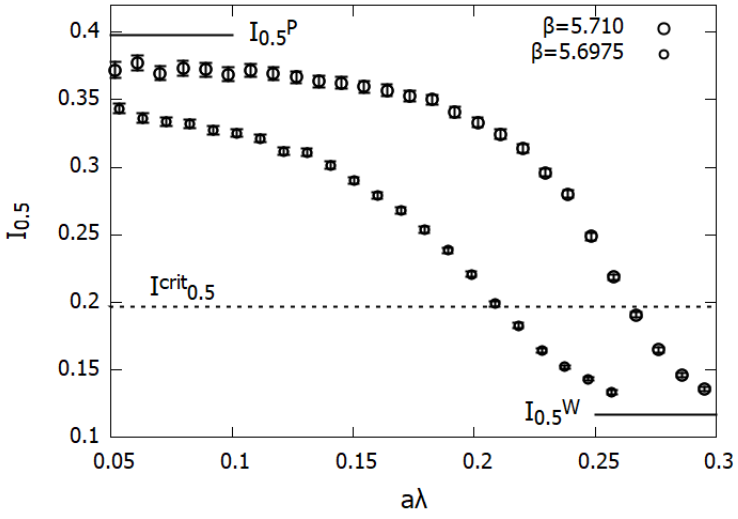

Figure 3.7: The quantity $I_{0.5}$ as a function of the eigenvalues calculated on lattices with spatial volume $V = 40^3$ and temporal extent $N_t = 4$ at two different values of the inverse gauge coupling $\beta = 5.6975$ (smaller circles) and $\beta = 5.710$ (larger circles).

We calculated the mobility edge for at least two different spatial volumes at each β (shown in table 3.1) to make sure that the change in the value of λ_c caused by finite sizes is smaller than the statistical error, which we calculated by the bootstrap method [39]. If λ_c only changed within the statistical error we stopped increasing the spatial volume of the lattice and accepted the value corresponding to the largest volume as the mobility edge. Figure 3.5 shows the function $I_{0.5}(\lambda)$ for different spatial volumes. It can be seen that the transition from localized to extended modes becomes sharper as the volume is increased.

As we went closer to the transition we needed to simulate lattices with larger spatial volumes (as it can be seen in table 3.1), because our experience showed that the correlation length increased as we went closer to the critical point. Thus the mobility edge calculated at different volumes showed greater finite size deviation from each other. We can expect that by looking at the the function $I_{0.5}(\lambda)$ close to the critical point. In this case correlations distort the function $I_{0.5}(\lambda)$, therefore the transition in the spectrum became flatter. This is illustrated in figure 3.7, where we calculated the quantity $I_{0.5}$ using lattices with spatial volume $V = 40^3$ but simulated at two different values of β. At the lower value of the inverse gauge coupling, corresponding to lower temperature, the function shows greater deviation from $I^P_{0.5}$ than in the case of higher β. This difference in the deviations basically disappears higher up in the spectrum, as the function approaches $I^W_{0.5}$.

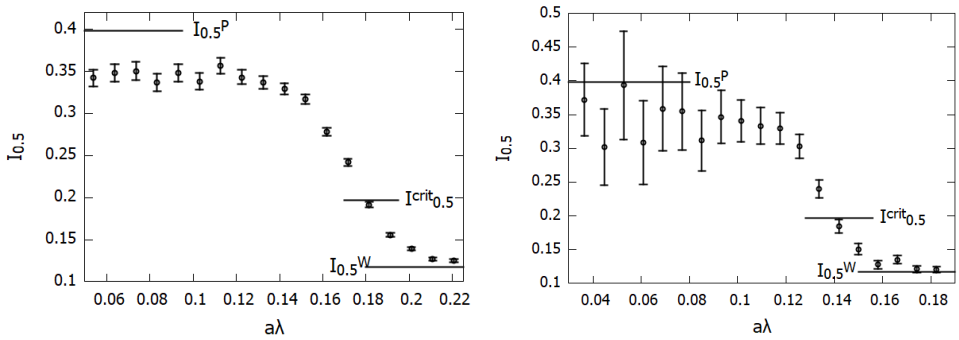

(a) (b)

Figure 3.8: In figure (a) the quantity $I_{0.5}$ is shown as a function of the eigenvalues, calculated on lattices with temporal size $N_t = 6$ and volume $V = 40^3$ at inverse gauge coupling $\beta = 5.92$. In figure (b) the same function is shown for lattices with temporal size $N_t = 8$ and volume $V = 56^3$ at $\beta = 6.1$.

We calculated λ_c in the same way as it was described above, for lattices with finer resolution, i.e. larger temporal extents ($N_t = 6$ and $N_t = 8$). The function $I_{0.5}(\lambda)$ was similar in these cases to the one in the $N_t = 4$ case. Two typical graphs are shown in figure 3.8 for lattices with temporal size $N_t = 6$ (left panel) and 8 (right panel). As we decreased the lattice spacing the lowest part of the spectrum became more depleted. It is visible in figure 3.8b (the highest resolution), that the statistics is smaller and therefore the errors are larger in bins at the lowest end of the spectrum. Unfolding works well for dense enough spectra, therefore we had to make sure that in bins that were relevant to our calculations, were enough eigenvalues for unfolding to give correct results. We ensured this by calculating the mean level spacing after unfolding in each bin and checked whether it really was close to unity.

So far we have seen how to determine the mobility edge in the spectrum of the staggered Dirac operator. Next we have to track its change as a function of the inverse gauge coupling, that we used to set the temperature of the system. In the following section I give our main results of the critical point of localization and compare it to that of the deconfining transition.

3.2.3 Critical point of localization

Our final step is to determine the critical temperature or, in our case of the quenched theory, the analogously used critical inverse gauge coupling of localization. Previously we have seen how to calculate the mobility edge at a fixed value of the inverse gauge coupling. Then we calculated λ_c at several values of β, just above the critical point of the deconfining transition, as we expect the localization transition to happen somewhere close to it. Thus we determined several points of the function $\lambda_c(\beta)$ numerically. Values of the mobility edge are shown in appendix A in table A.1.

Now we are interested in the value of β where the mobility edge reaches zero, i.e. where all the localized modes disappear from the spectrum. This value is the critical inverse gauge coupling for localization β_c^{loc}, which can be determined by solving equation (3.4). To this end we approximated the dimensionless function $a\lambda_c(\beta)$ with a power

fuction

$$a\lambda_c(\beta) \approx p_1(\beta - \beta_c^{loc})^{p_2}, \tag{3.8}$$

where p_1, p_2 and β_c^{loc} are parameters. This approximation is motivated by the fact that we examined the function $\lambda_c(\beta)$ in a relatively small interval close to the critical point of the transition. However, we had to keep in mind that fitting this function on the data is only valid in a range that is restricted from both the lower and the upper end. The point closest to the critical gauge coupling was chosen by the criterion, that the largest volume used in our simulations was large enough to keep the finite size effects under control. If the correlation length was too large, compared to the size of the lattice, the mobility edge had greater uncertainty due to finite volume effects, than the statistical error. In this case mobility edge values calculated from different volumes were not compatible within the statistical error. We had to omit those data points for which this was true. On the other end of the interval we could not go too far up with β, because the approximation (3.8) is only valid in a finite interval. We included the the largest number of points we could, while the fit described the data well enough. For this we measured the goodness of the fit with the reduced chi square

$$\chi_r^2 = \frac{1}{N_d - N_f} \sum \frac{(\lambda_c^{(d)}(\beta) - \lambda_c^{(a)}(\beta))^2}{\sigma_{(d)}^2}, \tag{3.9}$$

where $\sigma_{(d)}^2$ is the variance of the data, the denominator of the first term is the number of degrees of freedom, which is calculated by reducing the number of data points N_d with the number of fit parameters N_f. The summation goes over all data points that are involved in the fit, the measured value of the mobility edge is denoted by $\lambda_c^{(d)}(\beta)$ and the analytic approximation that we fit on the data is $\lambda_c^{(a)}(\beta)$. We aimed for the value of χ_r^2 to be close to one, which shows that the fit describes the data well. We shifted the upper end of the interval to include higher and higher values of β. We did this until χ_r^2 reached an acceptable value close to one and further increasing β made the fit worse. The parameters, the fit range that we used and the value of the reduced chi square are shown in table 3.2.

We repeated this procedure for three different lattice resolutions and for each we determined the parameter β_c^{loc}, where λ_c becomes zero. The fit on the data using the function (3.8) is shown in figure 3.9 for the three different lattice resolutions. In the figure only those points are shown, which we included in the fit interval.

N_t	β_c^{loc}	p_1	p_2	fit range (β)	χ_r^2
4	5.69245(17)	0.563(2)	0.1861(6)	5.695-5.71	0.31
6	5.8935(16)	0.320(1)	0.1580(8)	5.91-5.96	0.40
8	6.057(4)	0.233(2)	0.164(4)	6.08-6.18	0.49

Table 3.2: Parameters of the fit p_1, p_2 and β_c^{loc} with their errors indicated in the brackets, shown for three different temporal lattice sizes $N_t = 4, 6$ and 8. The fit range in β and the quantity χ_r^2 are also shown.

N_t	β_c^{deconf}	β_c^{loc}
4	5.69254(24)	5.69245(17)
6	5.8941(5)	5.8935(16)
8	6.0624(10)	6.057(4)

Table 3.3: The main results for the critical inverse gauge coupling of localization compared to that of deconfinement [40] with their errors in the brackets, at three different temporal lattice sizes.

We calculated the uncertainty of the critical value of localization in the following way. We generated random data points independently for each β with Gaussian distribution. For the generation we chose the mean of the distribution to be the mobility edge, measured on the lattice, and the standard deviation was the square root of the variance of λ_c. The generation of random data and fitting the function to it were done by using a code where we implemented the nonlinear least-squares Levenberg–Marquardt algorithm [41, 42]. We calculated the value where the mobility edge reached zero for several different randomly generated data sets. From this data we calculated the standard deviation of β_c^{loc}, i.e. the error of the critical point of localization. The critical inverse gauge coupling depend on the lattice spacing, therefore we compared our results of β_c^{loc} to β_c^{deconf} [40] of the corresponding resolutions, calculated in the quenched theory. The main results of the localization critical point of this staggered study are shown in table 3.3. It can be clearly seen, that the localization transition coincides with deconfinement within the statistical error. To illustrate this, we show the critical inverse gauge couplings with their error in figure 3.10.

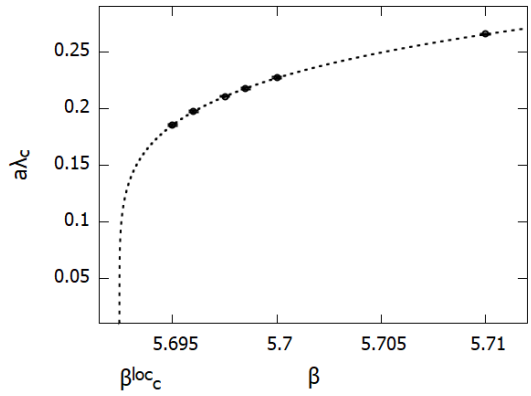

(a)

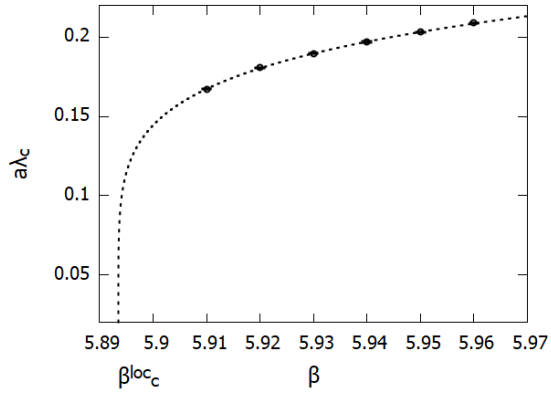

(b)

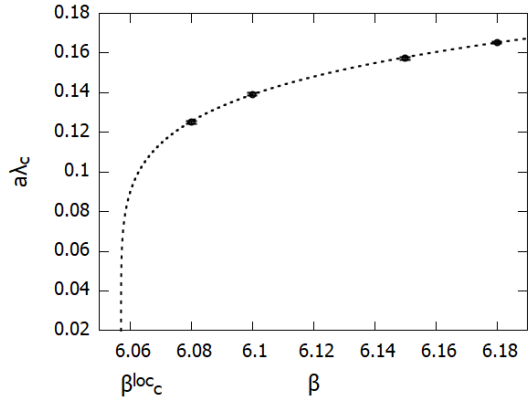

(c)

Figure 3.9: The mobility edge as a function of the inverse gauge coupling with a fit to the data (dashed line), for temporal size $N_t = 4$ (figure (a)), $N_t = 6$ (figure (b)) and $N_t = 8$ (figure (c)).

Our results for β_c^{loc} are discussed in References [11,12] and also form the first thesis point. We have shown that deconfinement and localization happen precisely at the same temperature in the quenched theory. It is very likely that the occurrence of the two phenomena coincide also in the continuum limit, as the critical values are compatible for three different lattice spacings. In full QCD the question whether deconfinement and localization coincide is not well defined, as the transition is only a crossover. However, the fact that they happen at the same temperature in the quenched theory indicates that there is a strong connection between these phenomena. Moreover, one of them may induce the occurrence of the other. To make this evidence stronger we investigated this question with another discretization of the fermionic action that has exact chiral symmetry on the lattice. Details of the calculations with the Overlap operator is discussed in the following sections.

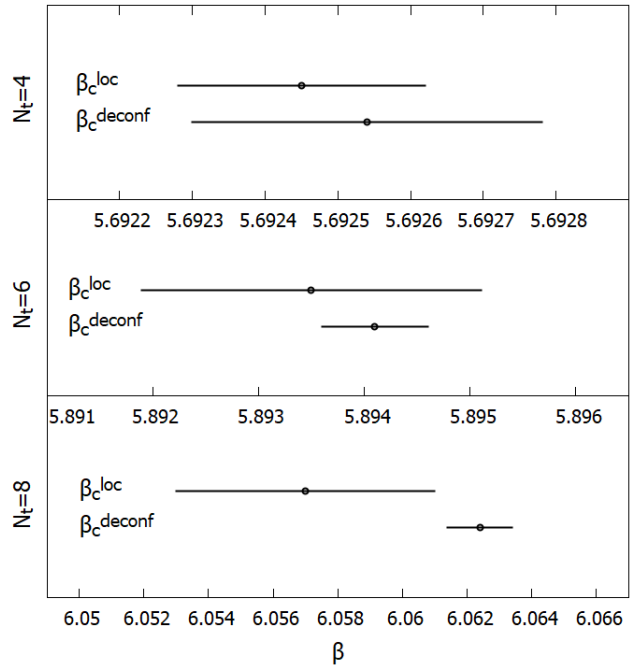

Figure 3.10: Illustration of the critical inverse gauge couplings of localization (upper dots) and deconfinement (bottom dots) with their errors (horizontal lines), shown for three different temporal lattice sizes $N_t = 4, 6$ and 8, for each we used different scales in β on the horizontal axis.

3.3 Localization with Overlap fermions

Our results of the critical inverse gauge coupling of localization, calculated with staggered quarks, showed that the temperature, where localization occurs, agrees well with the critical temperature of deconfinement. However, the zero mass staggered Dirac operator does not have exact chiral symmetry for finite lattice spacings as continuum quarks do. Localization affects the lowest part of the spectrum of the Dirac operator, which is particularly sensitive to the chiral properties of the Dirac operator in use (described in more details in section 2.3.3). Therefore there is a possibility that the incomplete chiral symmetry of the staggered Dirac operator produce localization of eigenmodes differently than a Dirac operator that has exact chiral symmetry.

To find out whether this concern is real we repeated the determination of the critical inverse gauge coupling of localization with the overlap discretization. This Dirac operator has the advantage that it has exact chiral symmetry already for finite lattice spacing (discussed in section 2.3.3), just like it is for continuum quarks. Moreover, the couplings between the quark degrees of freedom (off-diagonal matrix elements of the Dirac operator) fall exponentially with distance in the case of the Overlap Dirac operator. It is in contrast with the staggered Dirac operator which only couples the neighboring quark degrees of freedom. As Anderson localizations in general depend on locality properties of the Hamiltonian [32], it is an interesting task to check whether the nonlocality has an effect on the localization of quarks with the overlap discretization.

3.3.1 Simulation details

In our overlap study, we followed the same procedure described in section 3.2.1 to determine the mobility edge and the critical inverse coupling of localization. We used the overlap Dirac operator D_{ov} (2.73) for our calculations, with Wilson kernel parameter $M_0 = -1.3$ (see section 2.3.3 for a detailed discussion of the overlap operator). Here we used the $N_t = 6$ set of lattice configurations that we generated for our staggered calculations. The parameters of the simulation, that we used in our study with the overlap Dirac operator, are gathered in table 3.5.

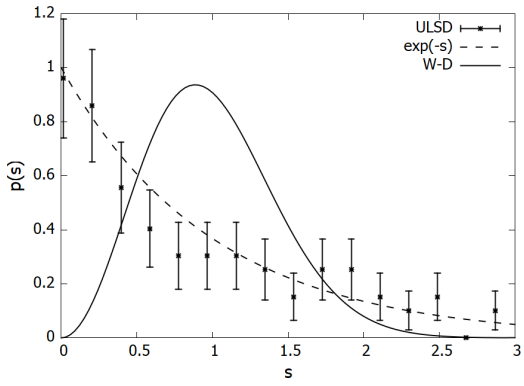

(a)

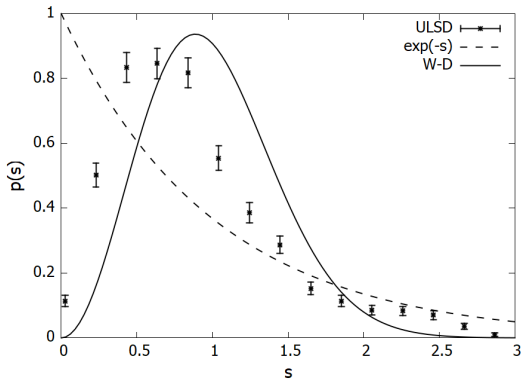

(b)

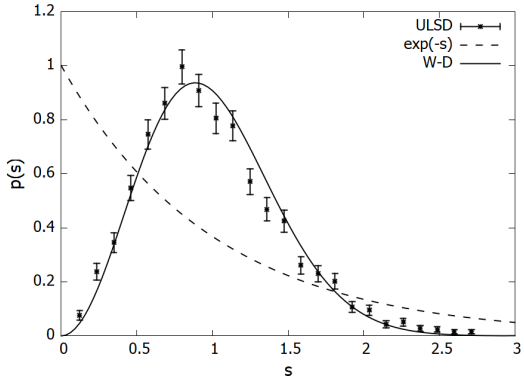

(c)

Figure 3.11: The probability density function of the unfolded eigenvalues. It is shown that the calculated data (dots) changes between Poisson distribution (dashed line) to the Wigner surmise (continuous line). The function is shown in three different spectral windows, at the lowest eigenvalues (figure (a)), at the critical region of the spectrum (figure (b)) and at the largest calculated eigenvalues corresponding to extended modes (figure (c)).

β	N_s	N_{cf}	N_{ev}
5.91	40	741	80
5.92	24	4668	25
	32	3823	50
	40	821	80
5.93	40	750	80
5.94	40	856	80
5.95	40	835	80
5.96	24	3915	25
	40	609	80

Table 3.4: Parameters of the simulation for lattices with temporal size $N_t = 6$. From left to right the Wilson plaquette gauge couplings (β), the size of the lattice in spatial direction (N_s), the number of the configurations (N_{cf}) and the number of eigenvalues computed for each configuration (N_{ev}) are listed.

To improve the properties of the overlap Dirac operator, we used hex smearing two times on the gauge links. On the smeared configurations, we determined the lowest eigenvalues of $D_{ov}^{\dagger}D_{ov}$, i.e. we the spectrum consisted of the square of the eigenvalues magnitudes, $|\lambda|^2$, of the overlap Dirac operator. For simplicity the eigenvalues of $D_{ov}^{\dagger}D_{ov}$ will be denoted by λ, from now on. We did not need to take the root of this spectrum, because we unfolded the spectrum before our calculations. Since taking the square of the eigenvalues is monotonic, it does not change the result of the unfolding procedure. As the overlap Dirac operator possesses exact chiral symmetry on the lattice, it has exact zero eigenvalues (discussed in section 2.3.3). We removed these eigenvalues from the spectrum before doing the statistical analysis, because unfolding cannot be applied on degenerate eigenvalues. This did not change our results, as the mobility edge is not influenced by the zero modes.

After the unfolding, we divided the spectrum into small bins and calculated the differences between the neighboring eigenvalues, i.e. the level spacings. For the details of tis process see appendix B. We calculated $I_{0.5}$ in each bin and tracked how the local ULSD changed through the spectrum from the exponential distribution (3.5) to the Wigner surmise (3.6). In figure 3.11 we show how the calculated distribution of the unfolded level spacings from the lattice data changes smoothly during the transition. We demonstrate it by choosing one bin from

the lowest end of the spectrum (top panel), one from the middle of the transition region (middle panel) and one that is in the region of extended modes (bottom panel). Similarly to our staggered study we used the quantity $I_{0.5}$, calculated as equation (3.7) with upper limit $s_0 = 0.508$. By using this parameter it is easy to monitor the change of statistics through the spectrum and detect the transition. A typical graph of $I_{0.5}(\lambda)$, calculated from the unfolded overlap spectra, is shown in figure 3.12.

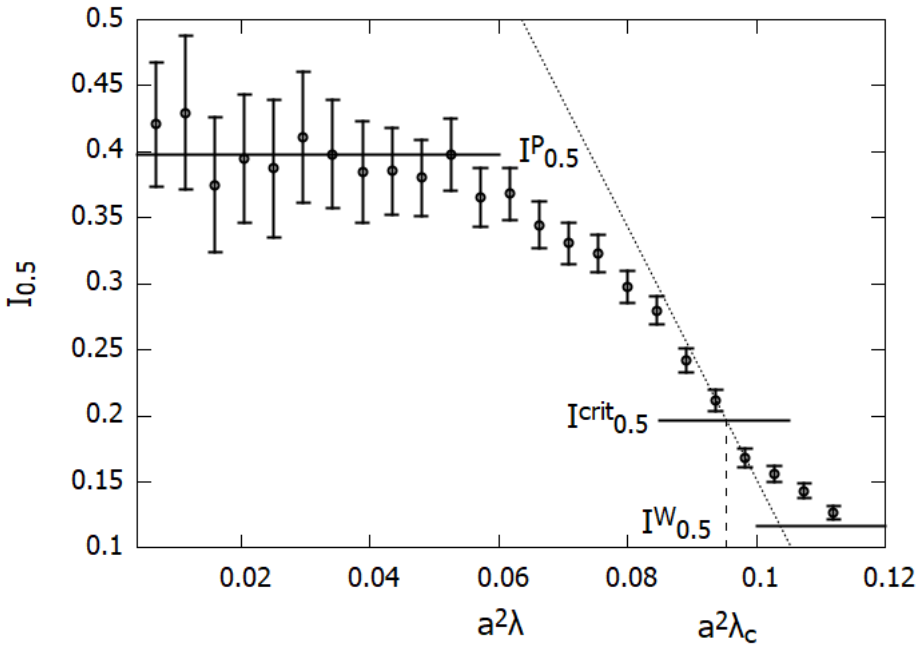

Figure 3.12: The quantity $I_{0.5}$ changing from te Poisson value (upper horizontal line) to the Wigner surmise (bottom horizontal line) as a function of the eigenvalues of $D_{ov}^{\dagger}D_{ov}$. The linear fit around the value $I_{0.5}^{crit}$ (densly dashed line) which we used to determine λ_c is also shown.

We determined the mobility edge by interpolating the function $I_{0.5}(\lambda)$ to its critical value, as it was described in the case of staggered fermions in section 3.2.2. In figure 3.12 we also illustrated the linear fit to the function, near the critical distribution, and the location in the spectrum where it intersects the value $I_{0.5}^{crit}$, which is the finite volume definition of λ_c. We determined λ_c for three different volumes $V = 24^3, 32^3$ and 40^3 (in lattice units) at inverse gauge coupling $\beta = 5.92$ (data are shown in table 3.5). For the two larger volumes, λ_c did change, only within the statistical error, that was calculated by the bootstrap method, sim-

ilarly to the case of staggered quarks. As $\beta = 5.92$ is one of the closest points to the critical point, the correlation length is large in this case. Therefore using the largest spatial volume $V = 40^3$ for the rest of our calculations at other values of β ensured that λ_c calculated on these lattices had an adequate value.

In the next section I present our main result obtained by using the spectra of the overlap Dirac operator to calculate the critical inverse gauge coupling of localization.

3.3.2 Critical point of localization

As it was described in the previous section, we determined the mobility edge in the spectra of the overlap Dirac operator using gauge configurations that we generated previously in our staggered study. Eigenvalue spectra were analyzed at six different values of the inverse gauge coupling in the QGP phase. Simulations were done close to the critical point of the deconfining transition, since we expect that localization happens at the same critical temperature in the quenched theory, as we previously verified it with staggered fermions. Calculated values of the mobility edge corresponding to different inverse gauge couplings are shown in appendix A in table A.2.

Our aim was to find the critical inverse gauge coupling, where the function $\lambda_c(\beta)$ vanishes. For this we extrapolated our data of the mobility edge, using the approximation (3.8), to find the zero of the function $\lambda_c(\beta)$. We selected the interval we fitted on by using the same criteria that we followed in the case of staggered fermions. The closest point to the transition was limited by the fact that we had to keep the finite size effects under control as the correlation length increased toward the transition. The farthest point from the transition was chosen by the criterion that, the use of the approximation (3.8) is only valid in a finite interval. The parameters of the fit and the χ^2_r, that we used to measure the quality of the fit are shown in table 3.5.

In figure 3.13 we demonstrate the lattice data for the mobility edge as a function of β and we also show the function that we used for the extrapolation. The error of β_c^{loc} was determined with the same method as it was described in section 3.2.3. The main result of our calculations for the critical inverse gauge coupling of localization in comparison to

β_c^{loc}	p_1	p_2	fit range (β)	χ_r^2
5.893	0.1741(35)	0.2082(63)	5.91-5.96	0.73

Table 3.5: Parameters of the function (3.8) that were fit on the data, the fit range that we used for the extrapolation and the reduced chi square are listed.

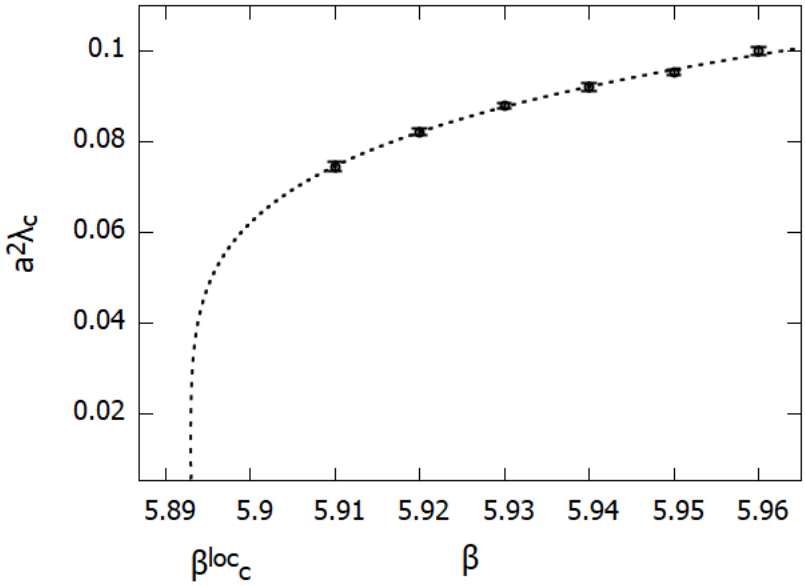

Figure 3.13: The mobility edge in the spectra of the overlap Dirac operator as a function of the inverse gauge coupling. The fit on the data (dashed line) using the function (3.8) is also shown.

that of deconfinement is the following

$$\beta_c^{deconf} = 5.8943(3) \qquad \beta_c^{loc} = 5.893(7),$$

where the errors are shown in the brackets. It can be seen, that the critical points of the two transitions are compatible within the numerical uncertainties. This agrees well with our results obtained with staggered quarks. This confirms that the two phenomena happen at the same temperature independently of the discretization. Thus it is very likely that there is a strong link between deconfinement and localization. Our overlap study is summarized in Ref. [13] and it forms the second thesis point.

3.4 Topology and localization

Topologically nontrivial gauge field configurations can have a strong effect on the spectrum of the Dirac operator. In the case of a Dirac operator with good chiral properties it leads to the appearance of degenerate eigenmodes that have zero eigenvalues. These zero eigenmodes can be related to regions in space-time with linear size $\rho \approx 1/3$ fm, where the gluonic field strength is locally very strong $A_{\mu\nu} \sim 1/(g\rho^2)$ (for a review see Ref. [8]). These topological lumps of the field strengths are called instantons (and antiinstantons). Gauge configurations with (anti)instantons satisfy the Euclidean equations of motion (see section 3.4.1), therefore significantly contribute to the path integral. Thus studying their effect on the physical quantities is an interesting task.

The presence of instantons has important consequences in QCD. On the one hand they are responsible for the anomalous breaking of the $U(1)$ axial symmetry. Another consequence is the spontaneously broken chiral symmetry at low temperatures. It can be intuitively understood from the following. In the regime of hadronic confinement (anti)instantons are believed to populate the QCD vacuum. According to the instanton liquid model their average density is one (anti)instanton per fm^4. Looking at the eigenvalue spectrum of the Dirac operator on an instanton liquid background, the lowest eigenvalues can be explained as approximate (anti)instanton zero modes. Thus we call this region of the spectrum the zero mode zone (ZMZ). Let us illustrate how (anti)instantons can be responsible for the ZMZ of the Dirac spectrum. Considering only one (anti)instanton there exists a fermion zero eigenmode with chirality $(-1)+1$. This zero eigenmode is localized on the (anti)instanton.

In the presence of an instanton and antiinstanton that are infinitely far apart, there are two exactly zero eigenmodes with opposite chirality. If their distance is gradually decreased the degeneracy of the eigenvalues splits up and there will be two complex conjugate eigenvalues, the magnitude of which are small but not zero. In the case of an instanton liquid at zero temperature, eigenmodes corresponding to these topological objects are delocalized and cause spontaneous chiral symmetry breaking, described by the Banks-Casher relation [10] that connects the low end of the Dirac spectrum to the chiral condensate $\Sigma \equiv \left\langle \bar{\psi}(x)\psi(x) \right\rangle$, that is the order parameter for chiral symmetry breaking. The connection

between Σ and the spectral density around zero is the following

$$\lim_{m\to 0}\lim_{V\to\infty}\Sigma(m,V,a) = \pi\lim_{\lambda\to 0}\lim_{m\to 0}\lim_{V\to\infty}\rho(\lambda,m) = \pi\rho(0) \tag{3.10}$$

where ρ is the spectral density, m, V and a are the fermion mass, spatial volume and the lattice spacing, respectively. This means that a finite spectral density at zero signals the spontaneous breaking of chiral symmetry and when the spectrum is depleted at the origin then chiral symmetry is restored.

In the high temperature regime, the topological susceptibility is rapidly falling, i.e. topological objects appear with a decreasing probability. The finite temperature counterparts of (anti)instantons the so called (anti)calorons are believed to form a dilute gas (we check this assumption in section 3.4.3) in the high temperature regime. In this case the interaction between calorons and anticalorons can be neglected and there will be localized eigenmodes with small magnitudes, coming from mixing instanton-antiinstanton zero eigenmodes. Thus the assumption naturally arises that the presence of topological objects at finite temperature might be responsible for the localization of quark eigenmodes at the low end of the Dirac spectrum. This interesting consequence of gauge field backgrounds with nontrivial topology motivated us to study the connection between localized eigenmodes and calorons.

In the next section I give a brief description of the theoretical background of the instantons. Then in section 3.4.2 I present our study about the relationship of (anti)caloron zero modes and localization and in section 3.4.3 I discuss the topic about how strong is the interaction between calorons and anticalorons above the critical point of the localization transition.

3.4.1 Instantons

Taking the semiclassical expansion of the path integral, the main contributions come from the classical theory corresponding to the local minima of the action. Hence it is interesting to check the possible solutions of the equations of motion, because they have important contributions to the path integral, thus in this way they govern the general behavior of the system. Since we work in Euclidean space when considering the path integral, it is crucial to discuss the Euclidean equations of motion. In pure gauge theory, which we simulated in our studies, an important class of the solutions to the Euclidean equations of motion

are the instanton solutions constructed by Atiyah, Drinfeld, Hitchin and Manin [43]. Instantons are gauge field regions localized in space-time that appear in topologically nontrivial gauge field configurations of the system. Next I give a brief summary of the construction of the instanton solution.

Let us consider the equation of motion following from the action of the continuum pure SU(3) gauge theory (2.34), given in section 2.2

$$D_\mu F_{\mu\nu} = 0, \tag{3.11}$$

where $D_\mu = \partial_\mu + A_\mu$ is the covariant derivative. Besides the trivial solution, $F_{\mu\nu} = 0$, one can find the minima of the action by rewriting it in the following way

$$\begin{aligned} S_G[A] &= \frac{1}{2g^2}\int d^4x\ tr[F_{\mu\nu}^2] = \\ &= -\frac{1}{4g^2}\int d^4x\ tr[F_{\mu\nu}^2 \pm \tilde{F}_{\mu\nu}^2] \pm \frac{1}{2g^2}\int d^4x\ tr[F_{\mu\nu}\tilde{F}_{\mu\nu}] = \\ &= -\frac{1}{4g^2}\int d^4x\ tr[F_{\mu\nu}^2 \pm \tilde{F}_{\mu\nu}^2] \pm \frac{8\pi^2}{g^2}Q, \end{aligned} \tag{3.12}$$

Here $\tilde{F}_{\mu\nu}$ is the dual field strength

$$\tilde{F}_{\mu\nu} = \frac{1}{2}\epsilon_{\mu\nu\alpha\beta}F_{\alpha\beta}, \tag{3.13}$$

where $\epsilon_{\mu\nu\alpha\beta}$ is the totally antisymmetric tensor. In the last step of (3.12), we used that the result of the second integral can be expressed in terms of an integer Q, called the topological charge

$$Q = \frac{1}{16\pi^2}\int d^4x\ tr[F_{\mu\nu}\tilde{F}_{\mu\nu}]. \tag{3.14}$$

The meaning of Q comes from the following picture. If we require that the action be finite, the field strength must fall to zero in the infinity of the Euclidean space-time. Therefore the vector potential has to be a pure gauge there

$$\lim_{|x|\to\infty} A_\mu(x) = g\partial_\mu g^{-1}, \tag{3.15}$$

where $g : S^3 \to SU(3)$, in the case of the strong force, is a mapping of the boundary three-sphere at infinity to the gauge group $SU(3)$. Such mappings belong to different homotopy classes, that are characterized by an integer, which is the topological charge (3.14) itself.

It follows from (3.12), that the gauge action is bounded from below

$$S \geq \frac{8\pi^2}{g^2}|Q|. \tag{3.16}$$

Equality is achieved if the first term in the last line of (3.12) is zero, i.e. when

$$F_{\mu\nu} = \pm\tilde{F}_{\mu\nu}, \tag{3.17}$$

which are the (anti)self-duality equations. If (3.17) is met, then the action is minimized. Therefore gauge configurations that satisfy the (anti)self-duality equation are solutions of the equation of motion as well. For a positive topological charge $Q > 0$, the self-duality equation is satisfied and the solutions are called instantons. For $Q < 0$, solutions satisfy the antiself-duality equation, hence they are called antiinstantons.

Following from the above, one can write the instanton action as

$$S_I = \frac{8\pi^2}{g^2}|Q|. \tag{3.18}$$

In finite temperature QCD, discussed in section 2.4, one works in the manifold $S^1 \times \mathbb{R}^3$ instead of $\mathbb{R}^4$. The solutions of the (anti)self-duality equations on such manifold are called (anti)calorons [44–46].

Finally let us write down the connection between the topological charge (3.14) and the zero eigenvalues of a chiral Dirac operator. The Atiyah-Singer index theorem [47] states that there is the following connection between the number of zero modes with a given chirality and the topological charge of the gauge field

$$Q = n_- - n_+, \tag{3.19}$$

where we denoted the number of zero modes with negative and positive chirality by n_- and n_+, respectively. If the Dirac operator explicitly breaks chiral symmetry, then there would not be zero eigenmodes as the deviation from zero of eigenvalues with the smallest magnitudes would be proportional to chiral symmetry breaking term.

By examining the zero mode density, it was shown on a charge one caloron background [48–50], that the fermion zero mode is localized on the caloron. If there are independent topological lumps carrying topological charge $|Q| = 1$, a zero eigenmode correspond to each. These eigenmodes mix in a nontrivial way, when the distance between the instantons is finite, as outlined in the previous section.

3.4.2 Localization on calorons

As it was described in the previous sections, zero and near-zero eigenmodes in the spectra of the Dirac operator can be related to topological lumps of the gauge field. These eigenmodes are localized on the topological lumps called calorons (in the case of finite temperature), that are acting as a potential well of the field strength. However gauge field configurations with such lumps of the field strength are usually not exact solutions of the Euclidean equations of motion, it would be more accurate to call them topological objects, but for simplicity we will use the notion caloron analogously.

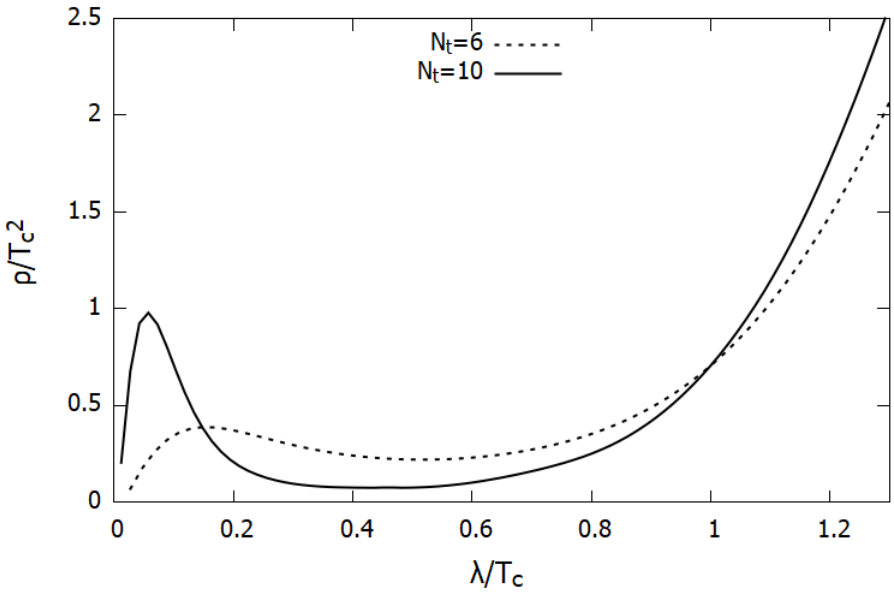

Figure 3.14: Spectral densities of the staggered Dirac operator at two different lattice resolutions, $N_t = 6$ at $\beta = 5.93$ (dashed line) and $N_t = 10$ at $\beta = 6.25$ (continuous line). The two different β values of the two resolutions correspond to the same physical temperature $T = 1.06T_c$. On the horizontal axis there are the dimensionless eigenvalues in units of the critical temperature.

Considering that the appearance of topological objects is accompanied by localized near-zero modes, the question arises whether all of the localized modes can be explained by mixed zero modes corresponding to calorons. The topology related eigenmodes can be studied by

calculating the eigenvalue spectra of a Dirac operator with good chiral properties. It was shown in a study of the overlap Dirac operator [51], that eigenmodes corresponding to calorons appear as a spike close to zero in the spectral density. This property of the spectral density offers us an opportunity to study eigenvalues of topological origin, because they could be separated from the rest of the spectrum.

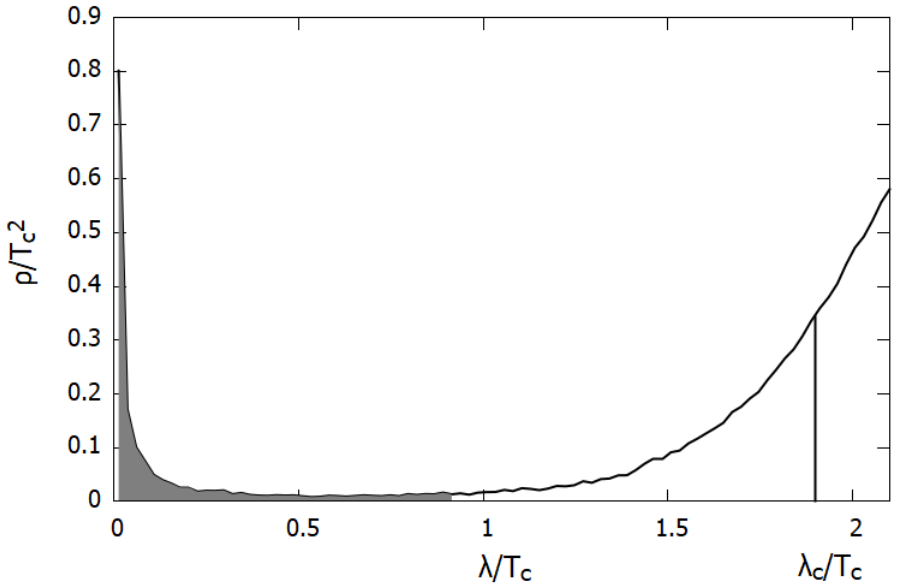

Figure 3.15: Spectral density of the overlap Dirac operator calculated on lattices with temporal extent $N_t = 6$ at $\beta = 5.93$, corresponding to temperature $T = 1.06T_c$. The dimensionless eigenvalues on the horizontal axis are shown in units of the critical temperature. The shaded area shows the region associated with the topology related localized modes. The vertical line shows the value of the mobility edge, i.e. how far all of the localized modes reaches up in the spectrum.

In our staggered study we also detected a near-zero spike in the spectra of the improved staggered Dirac operator, that presumably corresponds to caloron related near-zero eigenvalues. We found that the spectral density is similar in the case of the overlap operator, that we calculated on the $N_t = 6$ gauge configurations. In figure 3.14 we show the spectral densities of the staggered Dirac operator for two different lattice resolutions. It can be seen that the spike in the spectrum becomes more sharply isolated as the lattice spacing is decreased, while keeping the temperature fixed. Although the staggered Dirac operator

does not have exact chiral symmetry on the lattice, therefore it does not have exact zero eigenvalues, the two times stout smeared links and the fineness of our lattices already for $N_t = 6$ proved to be enough to resolve some of the caloron related eigenmodes. The spectral density of the $N_t = 6$ overlap operator is shown in figure 3.15.

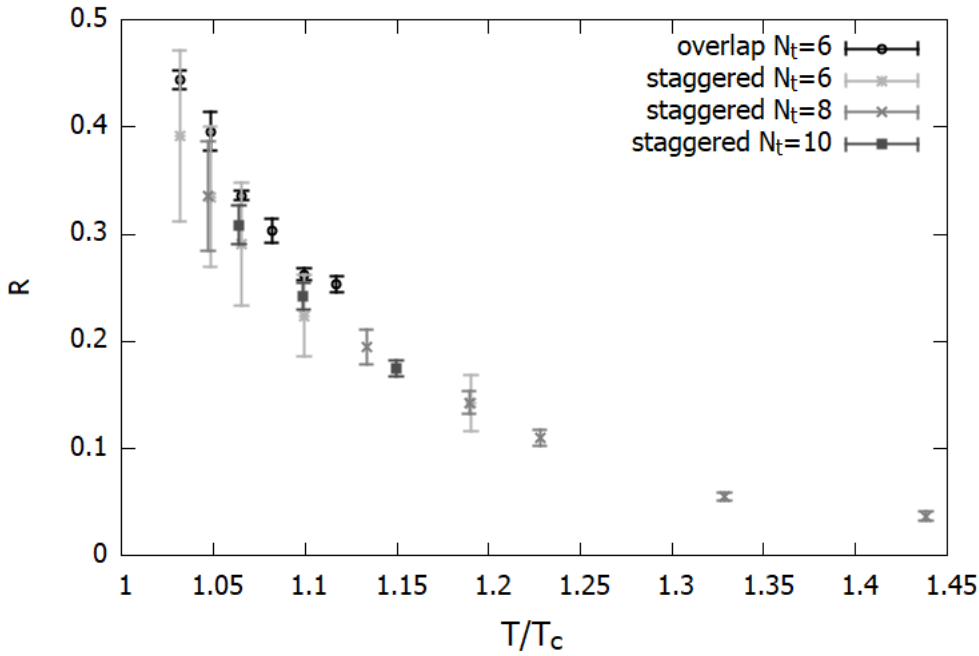

Figure 3.16: The dependence of the ratio of the number of the topology related localized modes and the total number of localized modes on the temperature. We show ratios that were calculated with staggered discretization at three different resolutions along with the ratio obtained with the overlap discretization.

We wanted to find out whether these topology related near-zero eigenvalues are responsible for the whole localization phenomenon. To this end we calculated the number of localized eigenmodes in the caloron related region of the spectrum and compared it to the number of all localized eigenmodes. As we calculated the mobility edge before, the number of all localized egenmodes could be easily determined by counting the number of eigenvalues that fell below λ_c. In figure 3.15 we show the location of the mobility edge in the spectral density of the overlap Dirac operator, calculated at $\beta = 5.93$. As calorons are responsible for the spike in the spectrum near the origin we considered those

eigenvalues, in the staggered spectral density, to be topology related, that fell below the minimum between the spike and the bulk of the spectrum. For the overlap spectrum we could develop a more precise method based on counting exact zero eigenvalues to identify the topology related eigenvalues. A detailed discussion of this novel method can be found in the next section.

After this we could calculate the ratio, R, of the number of the topology related eigenmodes n_{top} and the number of all localized eigenmodes n_{λ_c}. We calculated R at different values of the inverse gauge coupling, i.e. determined its temperature dependence, which is shown in figure 3.16. It can be seen that the topology related eigenmodes make up only a fraction of the number of all localized eigenmodes, moreover this fraction becomes smaller and smaller as the temperature is increased. Even by extrapolating R to the critical point of the localization transition, only a little more than half of the localized modes can be explained by near-zero modes localized on calorons. It can also be seen in figure 3.15 that the mobility edge is clearly farther up in the spectrum than the caloron related spike of the near-zero modes. The data of the ratios calculated from two different lattice discretizations and different lattice spacings are consistent, therefore it is very likely that this behavior persists in the continuum limit. These findings are discussed in References [11, 14] and this is the third thesis point.

3.4.3 Ideal topological gas above T_c

As the overlap operator is chirally symmetric on the lattice there are exact zero eigenvalues in its spectrum (see section 2.3.3). This makes it possible to precisely separate the caloron related spike from the rest of the eigenvalues. For this we use the relation (3.14) between the number of zero eigenvalues and the topological charge. By calculating the topological charge we can also determine the topological susceptibility

$$\chi_{top} = \frac{1}{V_4} \left\langle Q^2 \right\rangle , \tag{3.20}$$

where V_4 is the space-time volume of the lattice and $\langle . \rangle$ denotes averaging with the path integral.

The degeneracy of the zero eigenvalues of a caloron-anticalaron pair split up if they are at finite distance. Therefore exact zero eigenvalues can only be detected, when there are (anti)calorons that do not have

pair of opposite charge. This means that following from the definition (3.14), Q can be obtained by calculating the number of exact zero eigenvalues. Using this we can determine the number of all topological objects, i.e. the number of eigenvalues in the zero mode zone n_{zmz}. It can be calculated by adding the number of exact zero eigenvalues (the absolute value of the topological charge) to the number of near-zero eigenvalues n_{nz} in the spike

$$n_{zmz} = n_{nz} + |Q|. \tag{3.21}$$

If calorons and anticalorons occur independently in the gauge configurations, then n_{zmz} can be estimated. In this case the appearance of calorons and anticalorons is described by two independent and identical Poisson distributions with expectation value $(V_4\chi_{top})/2$. Then by calculating the distribution of the total number of calorons and anticalorons, i.e. $n_{zmz} = n_- + n_+$, it can be seen that it is also Poisson distributed

$$\begin{aligned} P(n_{zmz}) &= \sum_{n_-=0}^{\infty}\sum_{n_+=0}^{\infty} e^{-\frac{V_4\chi_{top}}{2}}\frac{(\frac{V_4\chi_{top}}{2})^{n_-}}{n_-!}e^{-\frac{V_4\chi_{top}}{2}}\frac{(\frac{V_4\chi_{top}}{2})^{n_+}}{n_+!} \\ &= \sum_{n_-=0}^{n_{zmz}} e^{-V_4\chi_{top}}\frac{(\frac{1}{2}V_4\chi_{top})^{n_{zmz}}}{n_-!(n_{zmz}-n_-)!} = e^{-V_4\chi_{top}}\frac{(V_4\chi_{top})^{n_{zmz}}}{n_{zmz}!}. \end{aligned} \tag{3.22}$$

From this, it can be seen that the expectation value for the number of topological objects is the following

$$\langle n_{zmz}\rangle = V_4\chi_{top}. \tag{3.23}$$

Equation 3.23 is true if (anti)calorons indeed behave like a dilute gas and their occurrence is independent. It is believed that at high temperatures this is the case and topological objects can be described by the dilute instanton gas approximation (DIGA). Using DIGA, semiclassical calculations of the temperature dependence of the topological susceptibility differ by an order of magnitude from results obtained in lattice simulations, even at temperatures much higher than the critical point $(5-10T_c)$ [52–54]. Thus it is reasonable to check the assumptions that DIGA is based on. These are that the one-instanton weight can be calculated in the semiclassical approximation and that the interaction between topological objects can be neglected i.e. they can be described as a dilute gas. Both assumptions are expected to be true at high temperatures. The first assumption was studied recently [55] and corrections were made for the semiclassical one-instanton calculations, but

these new results also have a 3σ discrepancy compared to the lattice results. This gives us another reason to checked whether (anti)calorons can really be described as a non-interacting gas at temperatures above T_c.

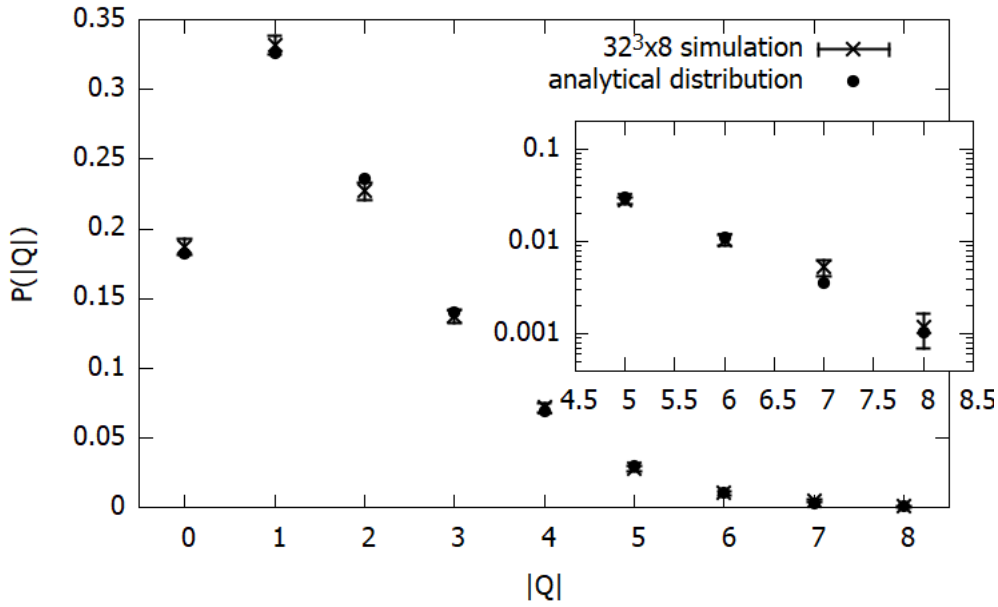

Figure 3.17: Probability density of the topological charge calculated analytically compared to the numerical data, calculated on lattices with volume $V = 32^3$ and temporal extent $N_t = 8$. As the probability density is symmetric in Q, we show the magnitude of the topological charge on the horizontal axis. On the inset the tail of the distribution can be seen on a logarithmic scale.

To test the idea that topological objects form a dilute gas at high temperatures, we calculated spectra of the overlap Dirac operator using quenched lattice configurations, with temporal extent $N_t = 8$ generated at $\beta = 6.09$. This corresponds to temperature $T = 1.045T_c$, i.e. the simulations are very close to the critical point of the finite temperature phase transition of the quarks. We generated lattice ensembles of 5000 configurations for two different spatial volumes $V = 24^3$ and 32^3 and another 600 configurations of a larger volume $V = 40^3$ to check finite volume effects of the Polyakov loop distribution. Similarly to our study of the localization critical point with the overlap Dirac operator (in section 3.3), used Wilson kernel parameter $M_0 = -1.3$ and determined the spectra on configurations with two times hex smeared gauge links. We

used configurations that fell in the real Polyakov loop sector as we did in our previous studies.

By calculating the number of exact zero eigenvalues in the overlap spectra calculated on each configuration, we could determine the topological sector the gauge configuration belonged to. Then we could check whether the distribution of the topological charge, determined from the lattice data, is compatible with the analytical prediction for non-interacting (anti)calorons. The analytical distribution of positive topological charge ($Q \geq 0$), i.e. the distribution of the difference of the number of calorons and anticalorons, can be calculated in the following way

$$P(Q) = \sum_{n_{zmz}=0}^{\infty} e^{-V_4\chi_{top}} \frac{(\frac{1}{2}V_4\chi_{top})^{Q+2n_{zmz}}}{(Q+n_{zmz})!n_{zmz}!} = e^{-V_4\chi_{top}} I_Q(V_4\chi_{top}), \quad (3.24)$$

where $I_Q(V\chi_{top})$ is the modified Bessel function of imaginary argument. We can extend the distribution for negative topological charges as $P(Q) = P(-Q)$ due to time reversal symmetry.

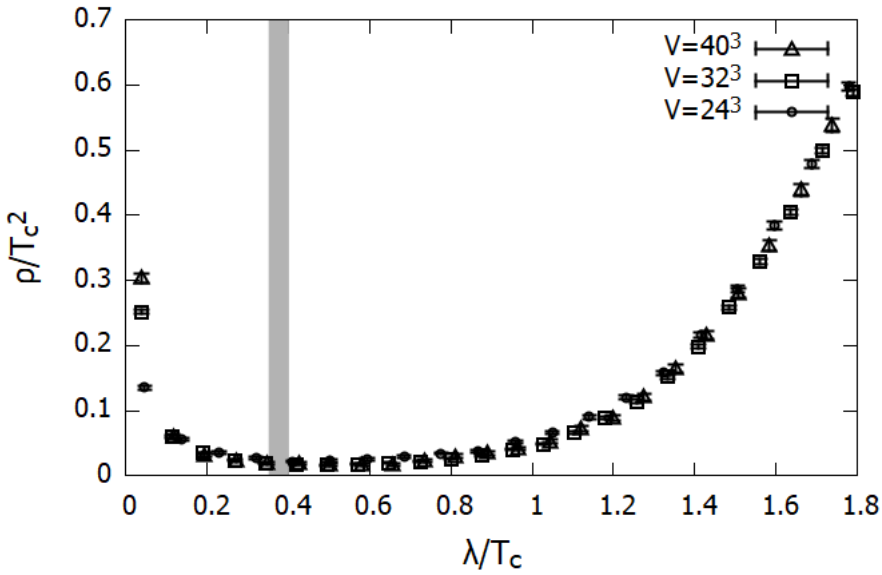

Figure 3.18: Spectral densities of the overlap operator, calculated on lattices with volumes $V = 24^3, 32^3$ and 40^3. The shaded region shows the cut with its error, under which all eigenvalues can be considered as topology related.

Now we compare the topological charge distribution calculated on

the lattice to the analytical distribution function of a free topological gas (3.24). We started the statistical analysis with the $V = 32^3$ lattice ensemble. The topological charge distribution is shown in figure 3.17, where we fit the analytical function with one parameter $V\chi_{top}$ to the lattice data. The errors were calculated with the bootstrap method. The reduced chi square of the fit was $\chi_r^2 = 0.85$, which indicates that the distribution of Q, measured on the lattice, corresponds to a free topological gas. Based on this, we checked the assumption that the spike in the spectral density corresponds to the topological objects of the gauge field. For this we needed to count the number of eigenvalues in the ZMZ. Using equation (3.23) we could determine the average number of topological objects. Thus we could choose a point in the spectrum λ_{zmz}, so that the average number of eigenvalues that fell below it satisfies (3.23). Using this requirement, we calculated λ_{zmz}, the eigenvalue that separates the zero mode zone from the bulk of the spectrum, which is in lattice units is the following

$$a\lambda_{zmz} = 0.045(6). \tag{3.25}$$

It can be seen in figure 3.18 that this value falls in the region of the spectrum where the spectral density is minimal.

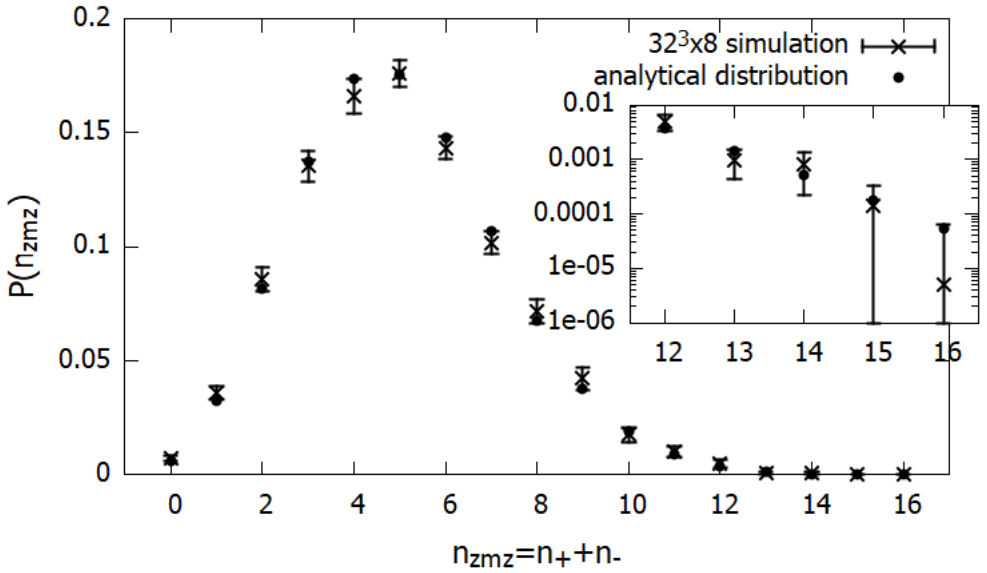

Figure 3.19: Analytical result of the probability density of the total number of topology related eigenmodes compared (n_{zmz}) to the probability density of n_{zmz}, calculated from $V = 32^3$, $N_t = 8$ lattice ensembles. The inset shows the tail of the distribution in logarithmic scale.

We calculated the number of eigenvalues on each configuration that fell below the value (3.25) and determined the distribution of the number of topological objects. We compared this result to the analytical prediction of a free topological gas (3.22). This can be seen in figure 3.19, where we did not have to do a parameter fitting as we already determined $V_4\chi_{top}$ from the distribution of the topological charge. The reduced chi square calculated from the comparison of the two functions took the value $\chi_r^2 = 0.62$. The good agreement between the lattice data and the analytical prediction indicates that the caloron related eigenmodes can be identified in the near zero spike of spectral density. Our results showed that topological objects can be described as a non-interacting gas already at a temperature as low as $T = 1.045T_c$.

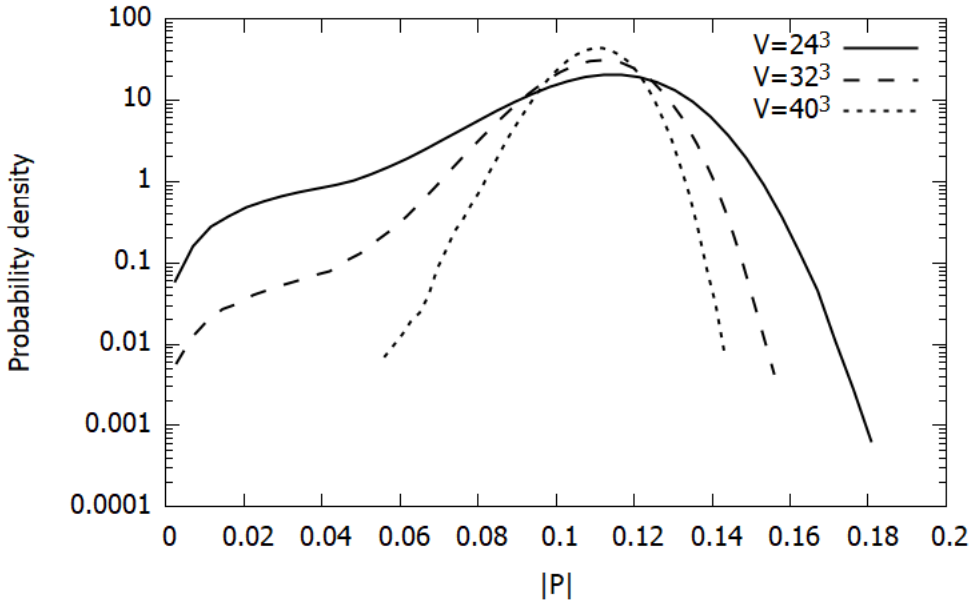

Figure 3.20: Probability densities of the magnitude of the Polyakov loop calculated from lattice ensembles with three different volumes $V = 24^3, 32^3$ and 40^3.

Since the temperature we used is in the vicinity of the critical point, we expect that the correlation length is large, hence large finite volume corrections could be needed. We saw this when we repeated the statistical analysis with lattices of a smaller spatial volume $V = 24^3$. By calculating the distribution of the topological charge and the total number of topological objects, we found that the lattice data deviates

significantly from the analytical predictions of a free topological gas. In fact the comparisons resulted in reduced chi squares $\chi_r^2 = 1.99$ for the topological charge distribution and $\chi_r^2 = 6.29$ for the distribution of n_{zmz}. We found that the reason for this is that the tunneling of the system between the three Polyakov loop sectors is more likely in smaller volumes. During the tunneling, the average Polyakov loop magnitude is smaller compared to its value on gauge configurations that fall in one of the $Z(3)$ sectors (the three Polyakov loop sectors are illustrated in figure 3.2a, in section 3.2.1). This distorts the Polyakov loop distribution in the direction of small magnitudes of Polyakov loop. We show the distributions of the Polyakov loop magnitude for different lattice sizes on figure 3.20. In the figure we also included the distribution on a larger volume $V = 40^3$.

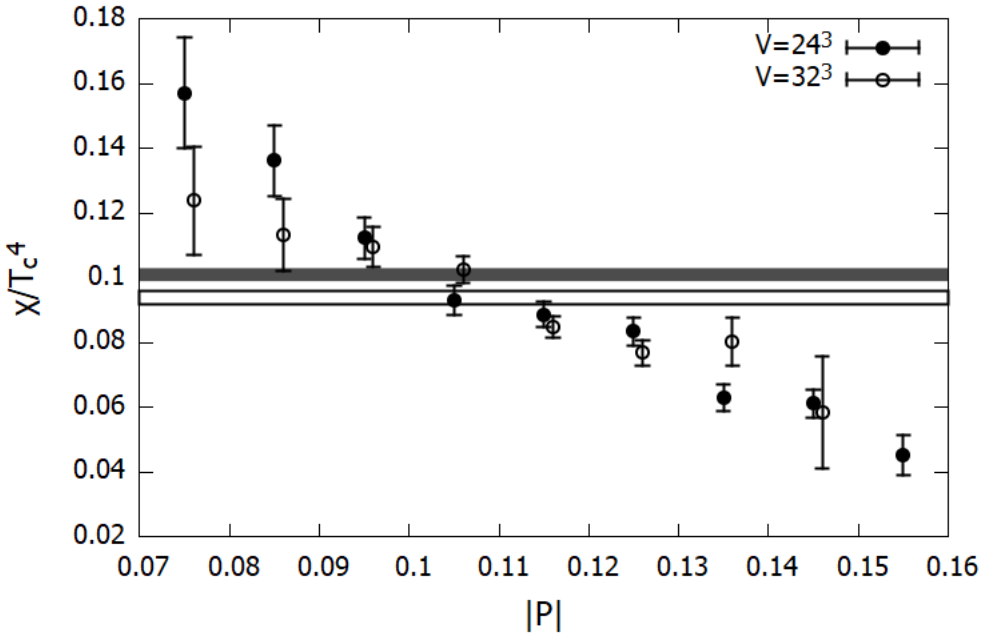

Figure 3.21: The dependence of the topological susceptibility on the magnitude of the Polyakov loop, shown for two different lattice volumes $V = 24^3$ and $V = 32^3$. The filled horizontal line shows the value of the topological susceptibility with its error, calculated from the full ensemble of $V = 24^3$ lattices. The blank horizontal line corresponds to the whole topological susceptibility of lattice ensembles with volume $V = 32^3$.

The average Polyakov loop affects the value of other physical observables, including the topological susceptibility and thereby the topological charge. To illustrate this we determined χ_{top} as a function of

the Polyakov loop magnitude $|P|$, by calculating Q^2 in intervals of size 0.01 in units of $|P|$. This can be seen in figure 3.21, where we show χ_{top} for spatial volumes $V = 24^3$ and 32^3 as a function of the Polyakov loop magnitude. The susceptibility increases for smaller values of $|P|$, therefore more tunneling that happen in smaller spatial volumes result in a larger topological susceptibility. In fig 3.21 we also show the susceptibilities with their errors calculated by the bootstrap method, for both volumes determined from the whole physical Polyakov loop sector. χ_{top} calculated on the smaller volume significantly differs from the larger volume result. Namely the topological susceptibility is larger because there are more lattice configurations with a smaller average Polyakov loop due to more tunneling events between the sectors. This means that on average there are more topological objects per unit volume in lattices with smaller spatial volume.

We have shown that the topological objects of the gauge field can be described as non-interacting caloron gas already just above the critical temperature. As this property becomes more pronounced at higher temperature we can conclude that the interaction between calorons is negligible in the whole high temperature phase. Based on this we could identify the caloron related part of the spectrum of a chiral Dirac operator. Our findings of the free caloron gas form the topic of the fourth thesis point and discussed in References [15, 16].

Chapter 4

Conclusions and outlook

In Chapter 3 we discussed the details of our studies about the localization transition and its connection to the topologically nontrivial gauge field. We determined the critical point of localization in the quenched theory, where deconfinement is a genuine first order phase transition. Thus in this case deconfinement has an unambiguously defined critical temperature, therefore we could answer the question whether the two phenomena precisely coincide. We found that indeed this is the case, in fact we verified it with two discretizations of the Dirac operator, of which one is chirally symmetric on the lattice. Results for decreasing lattice spacings strongly supports the idea that the two phenomena coincide in the continuum limit.

In full QCD the restoration of the spontaneously broken chiral symmetry also occurs during the crossover and it was suggested that deconfinement, chiral restoration and localization have a deeper physical connection. Our results were obtained in the quenched theory, the limit of infinitely large quark masses, in which case the chiral transition is not well defined. However, in the chiral limit it is expected to be a genuine first order phase transition, for which the corresponding order parameter is the chiral condensate. In the chiral limit we cannot define an order parameter for the deconfining transition, in contrast in the quenched approximation the Polyakov loop plays this role. We found that localization coincides with deconfinement in a model where it is a well defined first order phase transition. Therefore localization is more likely to be causally linked to deconfinement and not the chiral transition. However it would be interesting to calculate the critical point of localization also in the chiral limit and see whether it agrees with chiral transition.

The fact that in the high temperature phase of localization there is a nonzero spectral density near the origin, makes even more complicated to understand the connection between chiral restoration and localization. Although the low end of the spectrum is depleted in the high temperature phase, the topology related spike causes a finite spectral density at zero. This is a surprising phenomenon as a finite spectral density around zero signals spontaneous chiral symmetry breaking through the Banks-Casher relation [10]. We detected this spike with an improved staggered discretization and also in the spectrum of the overlap operator. Our work has shown that the accumulation of eigenvalues near zero is a topology originated phenomenon and the corresponding topological objects can be described as a non-interacting, dilute gas in the quenched theory. However, these topological objects probably deviate from the ideal caloron solution to such an extent that one cannot treat them semiclassically. This could explain the discrepancy between results of lattice calculations and perturbative calculations based on DIGA [55].

We have also shown that the topology related localized modes make up only a small fraction of the total number of localized quark modes. Moreover their contribution to the localized region of the spectrum become less significant as the temperature is increased. Therefore the phenomenon of quark localization cannot be explained by approximate zero modes localized on the topological lumps of the gauge field. These results of the topology related spike were obtained in the quenched approximation, however we expect that the qualitative behavior of the system is similar in full QCD with dynamical fermions. However, using dynamical quarks the fermion determinant might introduce an interaction between the topological lumps of the gauge field. Thus it would be interesting to check this idea in simulations with dynamical quarks using a chiral Dirac operator.

Summary

Strongly interacting matter has a finite temperature crossover from hadronic state to quark-gluon plasma, called deconfinement. Besides deconfinement two other phenomena happen in the crossover temperature region. These are the restoration of the approximate chiral symmetry and an Anderson-type localization of Dirac eigenmodes with the lowest eigenvalues. Even though there were studies in models similar to QCD where it was shown that localization and chiral transition coincide [56,57], the connection among the three phenomena that happen in the crossover is still not understood well. We studied this connection in another model similar to QCD, the quenched theory, where deconfinement is a genuine first order phase transition. This is the limit of infinitely large quark masses, when quarks cannot be generated from the vacuum. Therefore it is a pure SU(3) Yang-Mills theory.

We wanted to compare the critical temperature of deconfinement, that is known from the literature [40], to that of localization. Therefore we focused on the phenomenon of localization in our studies. In the high temperature phase the low end of the Dirac spectrum consists of localized eigenmodes, while higher up in the spectrum eigenmodes are delocalized. The value which separates these two regions is called the mobility edge (λ_c). Going toward the critical temperature, the mobility edge shifts toward the origin and at the critical point it disappears. At temperatures below this the whole Dirac spectrum consists of eigenmodes that are delocalized.

We determined the critical point of localization, i.e. where the mobility edge becomes zero. For this we generated lattice ensembles at different temperature points above the deconfining critical temperature and determined the temperature dependence of λ_c. At a fixed temperature, we determined λ_c by checking the unfolded level spacing distribution (ULSD) locally through spectrum of the staggered Dirac operator. Localized eigenmodes are independent from each other, therefore

they obey Poisson statistics. In contrast delocalized eigenmodes are described by Wigner-Dyson statistics, known from the random matrix theory [37]. We could detect this change in the statistics by dividing the spectrum into small bins and calculating a parameter of the distributions. We chose this parameter to be the integrated probability density function (I_{s_0}). We determined the function $I_{s_0}(\lambda)$ at a fixed temperature and calculated λ_c, which we defined in finite volume as the value where the quantity I_{s_0} reached the value corresponding to the critical distribution [38] $I_{s_0}(\lambda_c) = I_{s_0}^{crit}$.

We calculated λ_c at different temperature points close to the deconfining critical temperature, i.e. we determined the function $T(\lambda_c)$ close to the critical point. From this we determined the critical temperature of localization with extrapolation. We have done this procedure for three different lattice resolutions, and found that the disappearance of the localized eigenmodes coincides with the critical temperature of deconfinement in all the three cases. This suggests a strong link between the two phenomena, which is very likely to persists in the continuum limit.

The study discussed above was done by using the staggered discretization, which has a remnant chiral symmetry. The low end of the spectrum is sensitive to the chiral properties of the Dirac operator, therefore the discretization we used could have an effect on the properties of localization, which also affects the low end of the spectrum. Therefore we repeated our study of the localization critical temperature by using the overlap discretization of the Dirac operator, which has an exact chiral symmetry on the lattice. We found that localization and deconfinement coincide also in this case. This verifies our results obtained with the staggered Dirac operator and indicates that there is indeed a strong connection between localization and deconfinement, independently from the discretization.

The other aspect of our investigations was the examination of the role that topological objects of the gauge field play in the phenomenon of localization. On topologically nontrivial gauge field configurations there are localized lumps, called (anti)instantons, where the field strength is large. Instantons can be related to eigenmodes with small magnitude that are localized on these topological lumps. The instanton related eigenmodes appear as a spike in the spectral density around zero. We separated the part of the spectrum with topological origin

and compared the number of eigenvalues that fell in the instanton related region of the spectrum to the number of all localized eigenmodes (those eigenvalues that fell below the mobility edge). We found that the instanton related eigenvalues make up only a fraction of the number of all localized modes. This fraction becomes even smaller when the temperature is increased. Therefore we could conclude that small magnitude eigenmodes corresponding to instantons are not explaining the whole localization phenomenon.

We did the above described comparison of localized modes corresponding to the different regions of the spectrum, with the staggered as well as the overlap Dirac operator. In the staggered case we considered those eigenvalues to be instanton related that fell below the minimum between the spike at zero and the bulk of the spectrum. With overlap fermions we could use a more precise method to identify topology related eigenmodes. If we assume that the interaction of topological objects can be neglected, then the topological susceptibility contains enough information to calculate the average of the total number of instantons and antiinstantons. We only needed to know the topological charge, that can be easily determined in the case of the overlap Dirac operator, by calculating the number of exact zero eigenvalues. Then we could analytically determine the average of the total number of topological objects. From this we could find that point in the spectrum, below which all of the eigenmodes can be identified as instanton related.

The procedure described above only works if the assumption that the interaction between topological objects can be neglected, is true. Therefore we checked this assumption in the high temperature phase of localization. If the interaction can be neglected among topological objects, then the distribution of instantons and antiinstantons are described by two identical and independent Poisson distributions. Therefore we determined the distribution of the total number of topological objects and we could also calculate the distribution of the difference of the number of instantons and antiinstantons, i.e. the topological charge. We compared the analytical predictions to the data gathered from lattice simulations and found that they agree well, provided volumes were large enough for finite size effects to be negligible. Our calculations showed, that topological objects of the gauge field can be described as a non-interacting dilute gas, already at a low temperature of $T = 1.045T_c$.

Összefoglalás

Az erősen kölcsönható anyag rendelkezik egy véges hőmérsékletű átmenettel a színbezáró hadronikus fázisból a kvark-gluon plazma állapotba. Emellett az átmenet hőmérsékleti tartományában két másik jelenség is bekövetkezik. A királis szimmetria közelítőleges helyreállása és a legalacsonyabb sajátértékkel rendelkező Dirac-sajátmódusok Anderson-típusú lokalizációja. Habár voltak tanulmányok, amik kvantum-színdinamikához (QCD) hasonló modellekben megmutatták, hogy a királis átmenet és a lokalizáció egybeesik [56, 57], a kapcsolat a QCD átmenet során bekövetkező három jelenség között még nincs tisztázva. Mi ezt a véges hőmérsékletű átmenetet tanulmányoztuk, egy olyan QCD-hez hasonló modellben, amiben a kvark-gluon plazmába történő átmenet egy valódi elsőrendű fázisátalakulás. Ez az ún. quenched közelítés a végtelen nagy tömegű kvarkok határesete, ami azt eredményezi, hogy kvarkok nem tudnak létrejönni a vákuumból. Így ez egy tiszta (anyagmezők nélküli) SU(3) Yang-Mills elmélet.

Össze akartuk hasonlítani a kvark-gluon plazmába történő átmenet irodalomból ismert kritikus hőmérsékletét a lokalizáció kritikus hőmérsékletével. Így kutatásunkban a lokalizáció jelenségének vizsgálatára koncentráltunk. A magas hőmérsékletű fázisban a Dirac spektrum alját lokalizált módusokhoz tartozó sajátértékek alkotják, míg a spektrum magasabb régióiban a sajátmódusok térben kiterjedtek. Azt az értéket, ami elválasztja a spektrumban a lokalizált és kiterjedt módusokat egymástól mobilitási határnak (λ_c) nevezzük. Az átmenet kritikus hőmérséklete felé közeledve a mobilitási határ értéke csökken és egy kritikus hőmérsékleten nullává válik. A kritikus hőmérséklet alatti hőmérsékleti tartományban a spektrum összes sajátmódusa térben kiterjed.

Kiszámoltuk a lokalizáció kritikus pontját, ahol a mobilitási határ nullává válik. Ennek érdekében rács-sokaságokat generáltunk a kritikus hőmérséklet feletti tartományban és meghatároztuk λ_c hőmérsékletfüggését. Egy rögzített hőmérsékleti pontban λ_c meghatározása a szomszé-

dos sajátértékek univerzális távolságeloszlásának a spektrumbeli lokális vizsgálatán alapult. A lokalizált sajátmódusok függetlenek egymástól, így a hozzájuk tartozó sajátértékek Poisson eloszlást követnek. Ezzel ellentétben a kiterjedt módusokhoz tartozó sajátértékek eloszlását a véletlen mátrix elméletből ismert Wigner-Dyson statisztika [37] írja le. A statisztika változását a spektrumban úgy követtük nyomon, hogy a spektrumot kis intervallumokra daraboltuk és mindegyikben kiszámoltuk az eloszlásfüggvénynek egy általunk választott paraméterét. Ez a paraméter az integrált valószínűségi sűrűségfüggvény (I_{s_0}) volt. Meghatároztuk az $I_{s_0}(\lambda)$ függvényt egy rögzített hőmérsékleti pontban, ami alapján ki tudtuk számolni a λ_c adott hőmérséklethez tartozó értékét. A véges rácsmérethez tartozó mobilitási határt úgy definiáltuk, mint az az érték a spektrumban, ahol I_{s_0} eléri a kritikus eloszláshoz tartozó értéket [38] $I_{s_0}(\lambda_c) = I_{s_0}^{crit}$.

Kiszámoltuk λ_c értékét több különböző, kritikus hőmérséklethez közeli pontban, azaz meghatároztuk a $T(\lambda_c)$ függvényt kritikus hőmérséklethez közeli részét. Ebből extrapolációval kaptuk a lokalizáció kritikus hőmérsékletét. A számolást megismételtük három különböző rácsfelbontásnál és azt találtuk, hogy a lokalizált sajátmódusok eltűnése mindhárom esetben egybeesik a kvarkok kvark-gluon plazmába történő átmenetével. Az eredményeink alapján feltételezhetjük, hogy a lokalizáció és a hadronikus fázisátmenet között szoros kapcsolat van, ami nagy valószínűséggel a folytonos elméletben is megmarad.

A fentebb tárgyalt kutatásban staggered diszkretizációt használtunk, ami csak egy maradvány királis szimmetriával rendelkezik. A Dirac spektrum alja különösen érzékeny a Dirac operátor királis tulajdonságaira, ezért az általunk használt diszkretizáció befolyásolhatta a lokalizáció tulajdonságait, ami szintén a spektrum alját érinti. Ezért megismételtük a fentebb leírt kutatásunkat a Dirac operátor overlap diszkretizációját használva, ami egzakt királis szimmetriával rendelkezik a rácson. Azt találtuk, hogy a lokalizáció és a kvarkok véges hőmérsékletű átmenete ebben az esetben is egybeesik. Ez igazolja a staggered Dirac operátorral végzett tanulmányunk eredményeit, és azt jelenti, hogy a két jelenség között szoros kapcsolat áll fenn, diszkretizációtól függetlenül.

A kutatásunk egy másik aspektusa a topologikus objektumok lokalizációban betöltött szerepének vizsgálata volt. Nem triviális topológiával rendelkező mértéktér konfigurációkon vannak olyan régiók a téridőben, ahol a térerő lokálisan nagy a környezetéhez képest. Ezeket a

topológiai objektumokat (anti)instantonoknak nevezzük. Az instantonok kapcsolatba hozhatóak alacsony sajátértékekkel rendelkező módusokkal, amik az instantonokon lokalizálódnak. Ezek a sajátértékek egy nullához közeli csúcsként jelennek meg a spektrálsűrűségben. A kutatásunkban elkülönítettük a spektrum instantonokhoz köthető részét a többi sajátértéktől. Ezután összehasonlítottuk az instantonokhoz tartozó csúcsban található sajátértékek számát az összes lokalizált módus számával, azaz azon sajátértékek számával, amik a mobilitási határ alá estek. Azt találtuk, hogy az instantonok módusok sajátértékei csak egy töredékét teszik ki az öszes lokalizált módus számának. Ráadásul ez az arány még kisebbé válik, ahogy a hőmérsékletet növeljük. Ez alapján azt a következtetést vonhatjuk le, hogy instantonokhoz köthető kis sajátértékű lokalizált állapotokkal nem lehet teljes mértékben megmagyarázni a lokalizáció jelenségét.

A különböző spektrumbeli régiókhoz tartozó lokalizált módusok számának fentebb felvázolt összehasonlítását a staggered és az overlap operátor esetén is elvégeztük. A staggered spektrumban azokat a sajátértékeket tekintettük instanton eredetűnek, amik a spektrálsűrűségbeli csúcs és a magasabb sajátértékekhez tartozó spektrálsűrűség között megfigyelhető minimum alá estek. Az overlap operátor esetén egy pontosabb módszert tudtunk használni topológiai eredetű csúcs elkülönítésére. Ha feltesszük, hogy az instantonok közötti kölcsönhatás elhanyagolható, akkor a topológiai szuszceptibilitás elég információt tartalmaz ahhoz, hogy meghatározzuk az instantonok és antiinstantonok átlagos számát a mértéktér konfigurációkon. Ehhez elég volt tudni a topológiai töltést, ami könnyen meghatározható overlap operátor egzakt nulla sajátértékeinek megszámolásával. Ezután, ha analóg módon kiszámoljuk az összes topológiai objektum számának várható értékét, akkor a spektrumban meg tudjuk találni azt a pontot, ami alatt az összes sajátértéket instantonokhoz tartozó módusok sajátértékeivel azonosíthatjuk.

A fentebb felvázolt módszer akkor működik, ha az a feltevés, hogy az instantonok közötti kölcsönhatás elhanyagolható, igaz. Ezt a feltevést vizsgáltuk meg a magas hőmérsékletű lokalizált fázisban. Ha a topologikus objektumok közötti kölcsönhatás elhanyagolható, akkor az instantonok és antiinstantonok számának eloszlását két, egymástól független és azonos Poisson eloszlás írja le. Ez alapján ki tudtuk számolni az összes topologikus objektum számának eloszlását, valamint az instanton és antiinstanton szám különbségének, azaz a topologikus

töltésnek az eloszlását is meg tudtuk határozni. Az így kapott analitikus eredményeket összehasonlítottuk a rácsszimulációk eredményeivel és azt találtuk, hogy az analitikus és numerikus görbék mindkét esetben megegyeznek. Így megállapítottuk, hogy már a kritikus hőmérséklet közvetlen környezetében is helytálló az a kijelentés, hogy a topologikus objektumok olyan viselkedést mutatnak, mint egy kölcsönhatásoktól mentes, ritka gáz.

Appendices

Appendix A

The dependence of the mobility edge on β

$N_t = 4$		$N_t = 6$		$N_t = 8$	
β	$a\lambda_c$	β	$a\lambda_c$	β	$a\lambda_c$
5.695	0.18530(58)	5.91	0.16733(30)	6.08	0.16531(54)
5.696	0.19751(79)	5.92	0.18061(35)	6.1	0.15738(67)
5.6975	0.21056(31)	5.93	0.18975(46)	6.15	0.13919(86)
5.6985	0.21730(60)	5.94	0.19692(48)	6.18	0.12516(70)
5.7	0.22719(79)	5.95	0.20323(25)		
5.71	0.26544(42)	5.96	0.20887(39)		

Table A.1: Calculated values of the mobility edge (λ_c) at the sepctrum of the staggered Dirac operator, at different inverse gauge couplings (β). Errors are shown in the brackets. The three columns show data for different lattice temporal sizes (N_t).

β	$a^2\lambda_c$
5.91	0.07443(99)
5.92	0.08212(75)
5.93	0.08788(62)
5.94	0.09207(80)
5.95	0.09520(67)
5.96	0.09990(83)

Table A.2: Mobility edge (λ_c) at the spectrum of the overlap Dirac operator, at different inverse gauge couplings (β). Errors are shown in the brackets.

Appendix B

Details of the unfolded levels spacing calculation

We calculated the mobility edge from the unfolded Dirac spectrum. By unfolding, which means setting the spectral density unity through the whole spectrum, the fluctuations of the eigenvalues become universal. We did this by taking all the eigenvalues corresponding to an ensemble and replacing them with their rank in ascending order, then we normalized them by the number of configurations. In this way we could obtain universal quantities from the unfolded spectrum, like the unfolded level spacing distribution (ULSD).

We calculated the ULSD locally through the spectrum of the Dirac operator. For this we divided the spectrum into small bins. We determined the distribution of the level spacings in a given spectral window from those pairs of neighboring eigenvalues that belonged to that window. However it is arbitrary whether we consider a neighboring eigenvalue pair close to the edges of the interval to belong to it or not. By taking into account only those pairs of which both of the eigenvalues fall inside the interval, we would limit the size of the largest possible level spacing. This results in distorting the distribution of the level spacings by making an artificial cut at large values. To avoid this problem we stipulated that a neighboring eigenvalue pair belong to a given interval if the average of the two eigenvalues of the pair fell inside it. We did the division of the eigenvalues after unfolding the spectrum. For this we mapped the endpoints of the intervals in to the unfolded spectrum and did the division of the eigenvalues by considering these intervals. This ensures that our procedure is invariant when we do a monotonic mapping of the eigenvalues.

Bibliography

[1] S. Borsanyi, Z. Fodor, C. Hoelbling, S. D. Katz, S. Krieg, C. Ratti, and K. K. Szabo, "Is there still any T_c mystery in lattice QCD? Results with physical masses in the continuum limit III," *JHEP*, vol. 09, p. 073, 2010.

[2] J. Verbaarschot and T. Wettig, "Random matrix theory and chiral symmetry in qcd," *Annual Review of Nuclear and Particle Science*, vol. 50, p. 343–410, Dec 2000.

[3] A. M. Halasz and J. J. M. Verbaarschot, "Universal fluctuations in spectra of the lattice Dirac operator," *Phys. Rev. Lett.*, vol. 74, pp. 3920–3923, 1995.

[4] A. M. Garcia-Garcia and J. C. Osborn, "Chiral phase transition in lattice QCD as a metal-insulator transition," *Phys. Rev. D*, vol. 75, p. 034503, 2007.

[5] A. M. García-García and J. C. Osborn, "Chiral phase transition and anderson localization in the instanton liquid model for qcd," *Nuclear Physics A*, vol. 770, no. 3, pp. 141–161, 2006.

[6] M. Giordano, T. G. Kovacs, and F. Pittler, "Anderson localization in QCD-like theories," *Int. J. Mod. Phys. A*, vol. 29, no. 25, p. 1445005, 2014.

[7] A. M. F. and I. M. Singer, "The index of elliptic operators: V.," *Annals of Mathematics*, vol. 93, pp. 139–149, 1971.

[8] T. Schäfer and E. V. Shuryak, "Instantons in QCD," *Rev. Mod. Phys.*, vol. 70, pp. 323–426, 1998.

[9] T. Schäfer and E. V. Shuryak, "Instantons in qcd," *Reviews of Modern Physics*, vol. 70, p. 323–425, Apr 1998.

[10] T. Banks and A. Casher, "Chiral symmetry breaking in confining theories," *Nucl. Phys. B*, vol. 169, pp. 103–125, 1980.

[11] T. G. Kovacs and R. A. Vig, "Localization transition in SU(3) gauge theory," *Phys. Rev. D*, vol. 97, no. 1, p. 014502, 2018.

[12] R. A. Vig and T. G. Kovács, "Localization transition in SU(3) gauge theory," *PoS*, vol. LATTICE2018, p. 257, 2019.

[13] R. A. Vig and T. G. Kovacs, "Localization with overlap fermions," *Phys. Rev. D*, vol. 101, no. 9, p. 094511, 2020.

[14] T. G. Kovacs and R. A. Vig, "Localization and topology in high temperature QCD," *PoS*, vol. LATTICE2018, p. 258, 2019.

[15] R. A. Vig and T. G. Kovacs, "Free caloron gas in high temperature quenched QCD," *PoS*, vol. LATTICE2019, p. 192, 2019.

[16] R. A. Vig and T. G. Kovacs, "Ideal topological gas in the high temperature phase of SU(3) gauge theory," 1 2021.

[17] C. Gattringer and C. B. Lang, *Quantum chromodynamics on the lattice*, vol. 788. Berlin: Springer, 2010.

[18] T. DeGrand and C. E. Detar, *Lattice methods for quantum chromodynamics*. World Scientific, 2006.

[19] H. J. Rothe, *Lattice gauge theories: An Introduction*, vol. 43. World Scientific, 1992.

[20] C. Morningstar and M. J. Peardon, "Analytic smearing of SU(3) link variables in lattice QCD," *Phys. Rev. D*, vol. 69, p. 054501, 2004.

[21] P. H. Ginsparg and K. G. Wilson, "A remnant of chiral symmetry on the lattice," *Phys. Rev. D*, vol. 25, pp. 2649–2657, May 1982.

[22] H. Nielsen and M. Ninomiya, "A no-go theorem for regularizing chiral fermions," *Physics Letters B*, vol. 105, no. 2, pp. 219–223, 1981.

[23] M. Luscher, "Exact chiral symmetry on the lattice and the Ginsparg-Wilson relation," *Phys. Lett. B*, vol. 428, pp. 342–345, 1998.

[24] H. Neuberger, "Exactly massless quarks on the lattice," *Physics Letters B*, vol. 417, p. 141–144, Jan 1998.

[25] H. Neuberger, "More about exactly massless quarks on the lattice," *Physics Letters B*, vol. 427, p. 353–355, May 1998.

[26] T. G. Kovács, "Locality and topology with fat link overlap actions," *Phys. Rev. D*, vol. 67, p. 094501, May 2003.

[27] S. Capitani, S. Dürr, and C. Hoelbling, "Rationale for UV-filtered clover fermions," *Journal of High Energy Physics*, vol. 2006, pp. 028–028, nov 2006.

[28] A. Francis, O. Kaczmarek, M. Laine, T. Neuhaus, and H. Ohno, "Critical point and scale setting in SU(3) plasma: An update," *Phys. Rev. D*, vol. 91, no. 9, p. 096002, 2015.

[29] B. Kramer, A. MacKinnon, T. Ohtsuki, and K. Slevin, "Finite size scaling analysis of the anderson transition," *International Journal of Modern Physics B*, vol. 24, p. 1841–1854, May 2010.

[30] B. Kramer, A. MacKinnon, T. Ohtsuki, and K. Slevin, *Finite size scaling analysis of the Anderson transition*, pp. 347–360. 06 2010.

[31] T. Guhr, A. Muller-Groeling, and H. A. Weidenmuller, "Random matrix theories in quantum physics: Common concepts," *Phys. Rept.*, vol. 299, pp. 189–425, 1998.

[32] F. Evers and A. Mirlin, "Anderson transitions," *Rev. Mod. Phys*, vol. 80, pp. 1355 – 1417, 2008.

[33] M. Giordano, T. G. Kovacs, and F. Pittler, "Universality and the QCD Anderson Transition," *Phys. Rev. Lett.*, vol. 112, no. 10, p. 102002, 2014.

[34] J. J. M. Verbaarschot and T. Wettig, "Random matrix theory and chiral symmetry in QCD," *Ann. Rev. Nucl. Part. Sci.*, vol. 50, pp. 343–410, 2000.

[35] Y. Aoki, Z. Fodor, S. Katz, and K. Szabo, "The Equation of state in lattice QCD: With physical quark masses towards the continuum limit," *JHEP*, vol. 01, p. 089, 2006.

[36] G. W. Stewart, "A krylov–schur algorithm for large eigenproblems," *SIAM J. Matrix Anal. Appl.*, vol. 23, p. 601–614, Mar. 2001.

[37] J. Verbaarschot and T. Wettig, "Random matrix theory and chiral symmetry in qcd," *Annual Review of Nuclear and Particle Science*, vol. 50, no. 1, pp. 343–410, 2000.

[38] B. I. Shklovskii, B. Shapiro, B. R. Sears, P. Lambrianides, and H. B. Shore, "Statistics of spectra of disordered systems near the metal-insulator transition," *Phys. Rev. B*, vol. 47, pp. 11487–11490, 1993.

[39] B. Efron, "Bootstrap Methods: Another Look at the Jackknife," *The Annals of Statistics*, vol. 7, no. 1, pp. 1 – 26, 1979.

[40] A. Francis, O. Kaczmarek, M. Laine, T. Neuhaus, and H. Ohno, "Critical point and scale setting in su(3) plasma: An update," *Phys. Rev. D*, vol. 91, p. 096002, May 2015.

[41] K. Levenberg, "A method for the solution of certain non – linear problems in least squares," *Quarterly of Applied Mathematics*, vol. 2, pp. 164–168, 1944.

[42] D. W. Marquardt, "An algorithm for least-squares estimation of nonlinear parameters," *Journal of the Society for Industrial and Applied Mathematics*, vol. 11, no. 2, pp. 431–441, 1963.

[43] M. F. Atiyah, N. J. Hitchin, V. G. Drinfeld, and Y. I. Manin, "Construction of Instantons," *Phys. Lett. A*, vol. 65, pp. 185–187, 1978.

[44] F. Bruckmann, D. Nogradi, and P. van Baal, "Instantons and constituent monopoles," *Acta Phys. Polon. B*, vol. 34, pp. 5717–5750, 2003.

[45] T. C. Kraan and P. van Baal, "Periodic instantons with non-trivial holonomy," *Nuclear Physics B*, vol. 533, p. 627–659, Nov 1998.

[46] C. Gattringer and S. Schaefer, "New findings for topological excitations in SU(3) lattice gauge theory," *Nucl. Phys. B*, vol. 654, pp. 30–60, 2003.

[47] M. F. Atiyah and I. M. Singer, "The index of elliptic operators: V," *Annals of Mathematics*, vol. 93, no. 1, pp. 139–149, 1971.

[48] C. Gattringer, E.-M. Ilgenfritz, B. V. Martemyanov, M. Müller-Preussker, D. Peschka, R. Pullirsch, S. Schaefer, and A. Schäfer,

"Searching for kvbll calorons in su(3) lattice gauge field ensembles," *Nuclear Physics B - Proceedings Supplements*, vol. 129-130, pp. 653–658, 2004. Lattice 2003.

[49] M. Garcia Perez, A. Gonzalez-Arroyo, C. Pena, and P. van Baal, "Weyl-dirac zero mode for calorons," *Phys. Rev. D*, vol. 60, p. 031901, Jun 1999.

[50] F. Bruckmann, M. Garcia Perez, D. Nógrádia, and P. van Baal, "Calorons and fermion zero-modes," *Nuclear Physics B - Proceedings Supplements*, vol. 129-130, pp. 727–729, 2004. Lattice 2003.

[51] R. G. Edwards, U. M. Heller, J. E. Kiskis, and R. Narayanan, "Chiral condensate in the deconfined phase of quenched gauge theories," *Phys. Rev. D*, vol. 61, p. 074504, 2000.

[52] S. Borsanyi, Z. Fodor, J. Guenther, K. Kampert, S. Katz, T. Kawanai, T. Kovacs, S. Mages, A. Pasztor, F. Pittler, J. Redondo, A. Ringwald, and K. Szabo, "Calculation of the axion mass based on high-temperature lattice quantum chromodynamics," *Nature*, vol. 539, pp. 69–71, Nov. 2016.

[53] C. Bonati, M. D'Elia, M. Mariti, G. Martinelli, M. Mesiti, F. Negro, F. Sanfilippo, and G. Villadoro, "Axion phenomenology and θ-dependence from n f = 2 + 1 lattice qcd," *Journal of High Energy Physics*, vol. 2016, Mar 2016.

[54] P. Petreczky, H.-P. Schadler, and S. Sharma, "The topological susceptibility in finite temperature qcd and axion cosmology," *Physics Letters B*, vol. 762, p. 498–505, Nov 2016.

[55] A. Boccaletti and D. Nógrádi, "The semi-classical approximation at high temperature revisited," *Journal of High Energy Physics*, vol. 2020, pp. 1–16, 2020.

[56] A. M. García-García and J. C. Osborn, "Chiral phase transition in lattice qcd as a metal-insulator transition," *Phys. Rev. D*, vol. 75, p. 034503, Feb 2007.

[57] M. Giordano, S. D. Katz, T. G. Kovács, and F. Pittler, "Deconfinement, chiral transition and localisation in a qcd-like model," *Journal of High Energy Physics*, vol. 2017, Feb 2017.